

Assessment of added mass effects on flutter boundaries using the Leishman–Beddoes dynamic stall model

J. Peiró^{a,*}, U. Galvanetto^{a,b}, C. Chantharasenawong^{a,c}

^aDepartment of Aeronautics, Imperial College London, South Kensington Campus, London SW7 2AZ, UK

^bDepartment of Structural and Transportation Engineering, Università degli Studi di Padova, 35131 Padova, Italy

^cDepartment of Mechanical Engineering, King Mongkut's University of Technology Thonburi, Bangkok, Thailand

Received 7 November 2008; accepted 9 April 2010

Available online 15 June 2010

Abstract

We consider the dynamics of a typical airfoil section both in forced and free oscillations and investigate the importance of the added mass terms, i.e. the second derivatives in time of the pitch angle and plunge displacement. The structural behaviour is modelled by linear springs in pitch and plunge and the aerodynamic loading represented by our interpretation of the state-space version of the Leishman–Beddoes semi-empirical model. The added mass terms are often neglected since this leads to an explicit system of ODEs amenable for solution using standard ODE solvers. We analyse the effect of neglecting the added mass terms in *forced oscillations* about a set of mean angles of incidence by comparing the solutions obtained with the explicit and implicit systems of ODEs and conclude that their differences amount to a time lag that increases at a constant rate with increases of the reduced frequency. To determine the effect of the added mass terms in *free oscillations*, we introduce a spring offset angle to obtain static equilibrium positions at various degrees of incidence. We analyse the stability of the explicit and implicit aeroelastic systems about those positions and compare the locations of the respective flutter points calculated as Hopf bifurcation points. For low values of the spring offset angle, added mass effects are significant for low values of the mass ratio, or the ratio of natural frequencies, of the aeroelastic system. For high values of the spring offset angle, corresponding to stall flutter, we observe that their effect is greater for large values of the mass ratio.

© 2010 Elsevier Ltd. All rights reserved.

Keywords: Aeroelasticity; Added mass effects; Dynamic stall; Nonlinear dynamics; Flutter boundaries; Stall flutter

1. Introduction

The coupling of the structural and aerodynamic terms to form the equations of motion of an aeroelastic system, such as a typical airfoil section, results in the appearance of acceleration terms, i.e. second derivatives in time of the pitch angle and plunge displacement, which we will refer to as *added mass terms*. Such notation is unconventional when compared with its customary use in the literature (Blevins, 2001), but their effects are of a similar nature to those of the “true” added mass and, even though referring to them as “added mass type terms” could be more appropriate, we will

*Corresponding author. Tel.: +44 2075945051; fax: +44 2075848120.

E-mail addresses: j.peiro@imperial.ac.uk (J. Peiró), ugo.galvanetto@unipd.it (U. Galvanetto), chawin.cha@kmutt.ac.th (C. Chantharasenawong).

Nomenclature			
		U^*	non-dimensional airspeed, $U^* = (2V/c\omega_0)$
		V	free-stream velocity
a	speed of sound	x_0	distance between aerofoil elastic axis and centre of mass
a_h	distance between mid-chord and aerofoil elastic axis in semi-chords	\mathbf{x}	vector of state variables of the aeroelastic system $\mathbf{x}' = \mathbf{f}(\mathbf{x}, \mathbf{x}')$
b	length of semi-chord, $b = \frac{1}{2}c$		
c	chord length		
C_C	chord force coefficient	<i>Greek symbols</i>	
C_D	drag coefficient	α	effective angle of incidence
C_L	lift coefficient	α_1	static stall angle of incidence
C_M	pitching moment coefficient about the elastic axis	ζ_ξ	nondimensional damping coefficient in plunge
C_N	normal force coefficient	ζ_θ	nondimensional damping coefficient in pitch
C_{N_1}	critical normal force coefficient	θ	geometric angle of incidence (pitch)
f	position of trailing edge separation as a fraction of chord length	θ_0	spring offset angle
\mathbf{f}	right-hand side of the aeroelastic system	μ	aerofoil to air mass ratio, $\mu = m/\rho\pi b^2$
h	vertical displacement (plunge)	ξ	nondimensional plunge displacement, $\xi = h/b$
\mathbf{J}	Jacobian matrix of the system, $\mathbf{J} = \partial\mathbf{f}/\partial\mathbf{x}$	ρ	density of air
k	reduced frequency, $k = \omega c/2V$	ω	forced oscillation frequency in pitch
M	free-stream Mach number	ω_ξ	aerofoil plunge motion natural frequency
q	nondimensional effective pitch rate, $q = \dot{\alpha}c/V$	ω_θ	aerofoil pitch motion natural frequency
r	distance between the elastic axis and the calculation point in semi-chords	$\bar{\omega}$	ratio of natural frequencies, $\bar{\omega} = \omega_\xi/\omega_\alpha$
r_θ	aerofoil radius of gyration		
Re	free-stream Reynolds number referred to the chord length	<i>Subscripts</i>	
S	nondimensional time, $S = t(V/b)$	f	values corresponding to the full system
t	time	s	values corresponding to the simplified system
(u,v)	components of the velocity in the chord-wise frame of reference	ξ	refers to plunge motion
		θ	refers to pitch motion

retain this terminology throughout the paper. These terms are often neglected in practice since this yields an explicit system of ODEs which is easier to solve with standard ODE solvers. Otherwise, an implicit system of ODEs must be solved which requires more sophisticated, and computationally more expensive, solvers.

The main aim of the paper is to investigate the effect of neglecting the added mass terms in aeroelastic systems. To simplify the analysis, we have chosen one of the simplest aeroelastic systems: the typical aerofoil section with pitch and plunge degrees of freedom. The aerodynamic loading on the aerofoil is represented by a semi-empirical model of dynamic stall based on the methods proposed by Leishman and Beddoes, both in indicial and state-space forms, in a series of papers by Beddoes (1976, 1983, 1984), Leishman and Beddoes (1986, 1989), Leishman and Nguyen (1988) and Crouse and Leishman (1992). Our version of the state-space model is described by Galvanetto et al. (2008) and in more detail by Chantharasanawong (2007). In the following, it will be referred to as the LB model. The structural model is deliberately chosen to be linear so as to ensure that the nonlinear behaviour is exclusively due to the aerodynamic loading.

The majority of analyses of stall-induced vibrations are carried out by time integration of the ODEs representing the aeroelastic system with a variety of semi-empirical dynamic stall models such as the ONERA¹ (Sarkar and Bijl, 2008; Mahajan et al., 1993), Gormont (Li and Fleeter, 2003), Leishman–Beddoes (Price and Fragiskatos, 2000; Galvanetto et al., 2007) or Gangwani (Price and Keleris, 1996) models to name but a few. However, such an approach is computationally unaffordable for the purposes of this study. On the other hand, similar investigations of stall flutter using the ONERA model (Tran and Petot, 1981) have been carried out by Dat and Tran (1983) through an analysis of the stability of small amplitude oscillations, by Tang and Dowell (1996) using an eigenvalue analysis and by Beedy et al.

¹References to the ONERA model in this paper correspond, more specifically, to the ONERA EDLIN version of the model.

(2003) via the harmonic balance method. A common feature of these methods is that the aerodynamic influence of the motion of the aerofoil in pitch and plunge is accounted for by replacing the geometric angle of incidence θ by $\theta + (1/V)(dh/dt)$, where h is the plunge displacement and V is the free-stream velocity. The implicit assumptions are that the angular variations due to the plunge motion are small and that the first and second temporal derivatives of θ can be neglected.

The aim of this work is to investigate the validity of such simplifications, i.e., neglecting the added mass terms, using the evaluation of flutter boundaries as a representative aeroelastic problem. Flutter boundaries are characterized for the purposes of this investigation as loci of Hopf bifurcations in the parameter space where there is a transition from a fixed point to a limit cycle oscillation. This reduces to an eigenvalue analysis of the governing equations of the dynamical system linearized about an equilibrium configuration. To explore the stability of the system from linear to stall flutter, we incorporate a *spring offset angle*,² as proposed by Tang and Dowell (1996), that will permit us to find equilibrium, or fixed, points of the aeroelastic system for a wide range of incidences. This analysis will also be used to assess and illustrate some of the difficulties associated to the analysis of piecewise smooth dynamical systems.

The rest of the article is organized as follows. Section 2 presents the equations of motion of the aeroelastic system with emphasis on the calculation of the effective angle of incidence and the pitch rate as they determine the aerodynamic forces and moments on the aerofoil section. It also discusses the simplifications to the model that result from neglecting the acceleration terms in pitch and plunge. These terms, which we refer to as added mass terms, are often neglected in the literature without any assessment of the errors introduced. Here we analyse these errors by comparing the aeroelastic behaviour of the typical aerofoil section obtained when the aerodynamic forces represented by the LB model include the added mass terms and when they are neglected. Section 3 presents first the verification of our version of the LB model against published experimental and computational data with a view to assess its ability to matched them, and to evaluate the magnitude of the matching errors. The discussion of the errors associated with neglecting the added mass terms is carried out in Section 4 for forced harmonic oscillations. Section 5 analyses the effect of the added mass terms for free oscillations of the aeroelastic system by identifying, using a linear stability analysis, the Hopf bifurcation points over a range of equilibrium angles of incidence. The conclusions of this study are given in Section 6.

2. Governing equations of the motion of the typical aerofoil section

The aeroelastic model discussed here is a typical aerofoil section with two degrees of freedom. The aerofoil can move in the vertical direction (plunge) and rotate in the plane (pitch), as shown in Fig. 1. The mechanical model consists of bending and torsional springs that are attached to the aerofoil model at the elastic axis, together with the relevant dampers. Only aerodynamic nonlinearities will be investigated here and therefore the structural response is assumed to be linear. In any event, the methods of analysis described here could be easily adapted to incorporate non-linear structural behaviour (Lee et al., 1999).

The section used is a NACA0012 aerofoil in a horizontal flow of undisturbed speed V , as shown in Fig. 1. The *plunge deflection* of the elastic axis is denoted by h , taken to be positive in the downward direction, and θ is the *geometric angle of incidence* about the elastic axis. This is the angle between the flow direction and the chord line and it is taken to be positive nose-up (clockwise according to Fig. 1). The chord length is denoted by c and the semi-chord by $b = \frac{1}{2}c$. The elastic axis is located at a distance $a_h b$ from the mid-chord position, while the mass centre is located at a distance $x_\theta b$ from the elastic axis. Both distances are positive when measured toward the trailing edge of the aerofoil.

The coupled bending-torsion equations of motion for the aerofoil have been derived in many textbooks, for example Fung (1993), and can be written in nondimensional form, see for instance Lee et al. (1999), as

$$\xi'' + x_\theta \theta'' + 2\zeta_\xi \frac{\bar{\omega}}{U^*} \xi' + \left(\frac{\bar{\omega}}{U^*}\right)^2 \xi = -\frac{1}{\pi\mu} C_L(S), \quad (1)$$

$$\frac{x_\theta}{r_\theta^2} \xi'' + \theta'' + 2\frac{\zeta_\theta}{U^*} \theta' + \frac{\theta}{U^{*2}} = \frac{(0.5 + a_h)}{\mu\pi r_\theta^2} [C_L(S)\cos\theta + C_D(S)\sin\theta] + \frac{2}{\pi\mu r_\theta^2} C_M(S), \quad (2)$$

where θ is the angle of incidence and $\xi = 2h/c$ is the nondimensional plunge displacement. The lift and drag coefficients of the aerofoil are denoted by C_L and C_D , respectively, and C_M represents the pitching moment coefficient about the elastic axis. The prime denotes differentiation with respect to the nondimensional time $S = t(2V/c)$. Other parameters in the equations of motion are: the ratio of natural frequencies, $\bar{\omega} = \omega_\xi/\omega_\theta$, the plunge (bending) natural frequency, ω_ξ ,

²Tang and Dowell refer to it as *initial pitch*, but we feel that the term *spring offset angle* describes it more accurately.

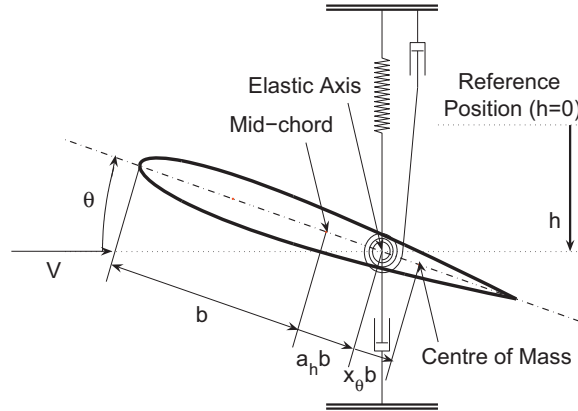


Fig. 1. Notation for a typical aerofoil section with two degrees of freedom: pitch, θ , and plunge, h .

the pitch natural frequency, ω_θ , the nondimensional damping coefficients in plunge and pitch, ζ_ξ and ζ_θ , respectively, the non-dimensional airspeed, $U^* = 2V/c\omega_\theta$, the aerofoil to air mass ratio, $\mu = m/\rho\pi b^2$, the aerofoil radius of gyration, r_θ , and the distance from elastic axis to centre of mass, x_θ .

The aerodynamic coefficients C_i ; $i = L, D, M$ are calculated using our interpretation of the state-space form of the LB semi-empirical dynamic stall model (Galvanetto et al., 2008; Chantharasenawong, 2007). The aerodynamic loading is given as a function of a vector of 12 components, the state variables of the system, denoted by $\mathbf{x}_a = [x_1, \dots, x_{12}]^T$. This vector is the solution of the system of ODEs

$$\mathbf{x}'_a = \mathbf{f}_a(\mathbf{x}_a, \alpha(\mathbf{x}_a), q(\mathbf{x}_a)), \quad (3)$$

where the symbols α and q denote the *effective angle of incidence* and *pitch rate*, respectively, and the aerodynamic coefficients are given by expressions of the form

$$C_i = C_i(\mathbf{x}_a, \alpha(\mathbf{x}_a), q(\mathbf{x}_a)), \quad i = L, D, M. \quad (4)$$

The equations of motion (1) and (2) can be written as a system of four first-order ODEs by assigning the pitch angle and plunge displacement and velocities to the vector of state variables

$$\mathbf{x}_e = [x_{13}, x_{14}, x_{15}, x_{16}]^T = [\theta, \theta', \xi, \xi']^T. \quad (5)$$

The resulting system will be written in abridged form as

$$\mathbf{x}'_e = \mathbf{f}_e(\mathbf{x}_e, C_L, C_D, C_M). \quad (6)$$

The structural and aerodynamic models can be combined to create a system of first-order ODEs which describe the aerofoil motion and is given by

$$\mathbf{x}' = \begin{Bmatrix} \mathbf{x}'_a \\ \mathbf{x}'_e \end{Bmatrix} = \begin{Bmatrix} \mathbf{f}_a \\ \mathbf{f}_e \end{Bmatrix} = \mathbf{f}(\mathbf{x}) = \mathbf{f}(\mathbf{x}, \alpha(\mathbf{x}), q(\mathbf{x})), \quad (7)$$

where $\mathbf{x} = [x_1, x_2, \dots, x_{16}]^T$.

The aeroelastic model requires the calculation of the effective angle of incidence, α , and the effective pitch rate, q . Using the notation of Fig. 2, in particular the velocity triangle in Fig. 2(c), the effective angle of incidence, in a frame of reference that moves with the aerofoil, is given by

$$\alpha = \tan^{-1}\left(\frac{v}{u}\right) = \tan^{-1}\left(\frac{V \sin \theta + \dot{h} \cos \theta + \dot{\theta} r b}{V \cos \theta - \dot{h} \sin \theta}\right), \quad (8)$$

where the overdot represents differentiation with respect to time, u and v are the components of the velocity in the chord-wise frame of reference, as depicted in Fig. 2(b), and $r b$ is the distance between the elastic axis and the calculation point. Notice that, if we take $r = 0$ and assume that θ is small, we recover $\alpha = \theta + \dot{h}/V$, which is the formula used in other analyses, e.g. Leishman (2006), Sarkar and Bijl (2008), Mahajan et al. (1993), and Price and Fragiskatos (2000).

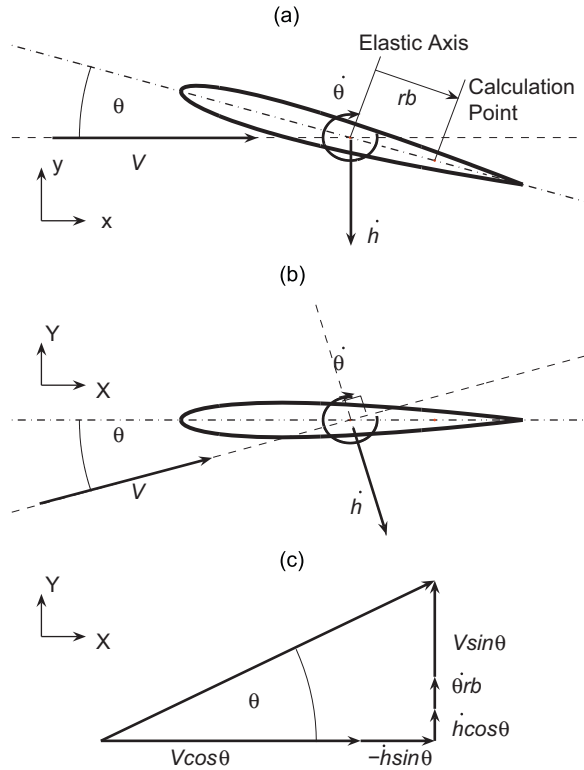


Fig. 2. A schematic of the typical aerofoil section and the velocity components in (a) the flow direction and (b) the chord-wise frame of reference. The resultant velocity triangle at the calculation point in the chord-wise frame of reference fixed to the aerofoil is shown in subfigure (c).

The nondimensional form of the effective angle of incidence is given by

$$\alpha = \tan^{-1} \left(\frac{\sin\theta + \zeta' \cos\theta + \theta' r}{\cos\theta - \zeta' \sin\theta} \right). \tag{9}$$

Note that for a pure pitch motion at the elastic axis, i.e. $\zeta' = 0$ and $r = 0$, the effective angle of incidence is reduced to $\alpha = \theta$.

The nondimensional pitch rate, denoted by q_f , is given by

$$q_f = \dot{\alpha} \frac{c}{V} = \left(\alpha' \frac{V}{b} \right) \frac{c}{V} = 2\alpha' = 2 \frac{LU' - UL'}{U^2 + L^2} \tag{10}$$

with

$$U = \sin\theta + \zeta' \cos\theta + \theta' r, \quad L = \cos\theta - \zeta' \sin\theta, \tag{11, 12}$$

$$U' = \theta' \cos\theta - \zeta' \theta' \sin\theta + \zeta'' \cos\theta + \theta'' r, \quad L' = -\theta' \sin\theta - \zeta' \theta' \cos\theta - \zeta'' \sin\theta. \tag{13, 14}$$

2.1. Simplifications obtained by neglecting the added mass terms

The effective pitch rate q_f contains the terms θ'' and ζ'' that we refer to as *added mass terms* in analogy with the classical analysis of fluid-induced accelerations. The inclusion of the effective pitch rate in the aeroelastic system ODEs through the LB model, results in the presence of these terms in the right-hand side of the equations leading to a system of the form

$$\mathbf{x}' = \mathbf{f}_f(\mathbf{x}, \mathbf{x}'), \tag{15}$$

where \mathbf{f}_f represents the right-hand side of Eq. (7) with $q = q_f$. This equation is an *implicit* system of ODEs, which will be referred to as the *full system*.

The definition of effective pitch rate could be simplified by neglecting the added mass terms θ'' and ζ'' from the effective pitch rate, as defined in Eqs. (13) and (14), to obtain

$$\hat{\alpha}' = \frac{L\hat{U}' - U\hat{L}'}{U^2 + L^2}, \tag{16}$$

where U and L are given by (11) and (12), respectively, and their derivatives (without the added mass terms) are

$$\hat{U}' = \theta' \cos\theta - \zeta' \theta' \sin\theta, \tag{17}$$

$$\hat{L}' = -\theta' \sin\theta - \zeta' \theta' \cos\theta. \tag{18}$$

Note that if the effective angle of incidence is evaluated at the elastic axis, i.e. $r = 0$, this expression conveniently reduces to $\hat{\alpha}' = \theta'$. The simplified effective pitch rate q_s is now given by

$$q_s = 2\hat{\alpha}' = 2\theta' \frac{1 + (\zeta')^2 + \theta' r(\sin\theta + \zeta' \cos\theta)}{1 + (\zeta')^2 + 2\theta' r(\sin\theta + \zeta' \cos\theta) + (\theta' r)^2}, \tag{19}$$

so the system of ODEs becomes

$$\mathbf{x}' = \mathbf{f}_s(\mathbf{x}), \tag{20}$$

where \mathbf{f}_s is given by the right-hand side of Eq. (7) with $q = q_s$. This will be referred to as the *simplified system*.

In this paper we compare the solutions of the implicit or full system (15) and those of the explicit or simplified system (20) to elucidate the effect of neglecting the added mass terms on the aeroelastic behaviour of aerofoil section. To study these effects we compare the solutions of both systems under forced and free oscillations and determine the range of parameters where the neglect of the added mass terms leads to the largest differences in behaviour. However, first we discuss the verification of our version of the LB model with a view to assess how well it reproduces available computational and experimental data.

3. Verification of the LB model

We use the LB model to predict the aerodynamic coefficients of normal force, $C_N = C_L \cos\theta + C_D \sin\theta$, and pitching moment, C_M , for an aerofoil harmonically oscillating in pitch with a reduced frequency $k = 0.10$. We consider two test cases with moderate and deep stall selected from the experimental data published by McCroskey (McCroskey et al., 1976; McAlister et al., 1983). The oscillatory motion in the moderate stall case is described by the equation $\alpha(S) = 10 + 10\sin(kS)$ and for the deep stall case we have $\alpha(S) = 15 + 10\sin(kS)$, where S is the non-dimensional time and α is given in degrees. The free-stream conditions correspond to a Reynolds number $Re = 3 \times 10^6$ and a Mach number $M = 0.3$. The static curves representing the variation of the aerodynamic coefficients with the angle of incidence were taken from the experimental data presented by McAlister et al. (1983). The numerical results from our implementation of the LB model³ are compared to the experimental data by McCroskey et al. (1976) and the numerical data from the original work by Leishman and Beddoes (1989).

The magnitude of the difference between the curves representing the computed and experimental time evolution of the aerodynamic coefficients will be measured by

$$\Delta C_i = \frac{\delta C_i}{C_{i_{\max}} - C_{i_{\min}}}, \quad i = L, N, M, \tag{21}$$

where δC_i is the root-mean-square, evaluated over one cycle, of the difference between the values calculated using our version of the LB model and the experimental data, and $C_{i_{\max}}$ and $C_{i_{\min}}$ are the maximum and minimum values, respectively, of the experimental aerodynamic coefficients during the cycle.

Fig. 3 presents that comparison for the moderate stall case. It shows that our implementation of the LB model produces results that are very close to the original version. Both versions of the LB model reproduce reasonably well the overall shape and magnitude of the experimental values of C_N and C_M except for the reattachment region where the largest errors occur. For this case, the magnitude of the errors calculated using Eq. (21) are $\Delta C_N = 6.4\%$ and $\Delta C_M = 4.6\%$.

³For fairness of comparison with the results of Leishman and Beddoes (1989), the simplified system in our version of the LB model is used.

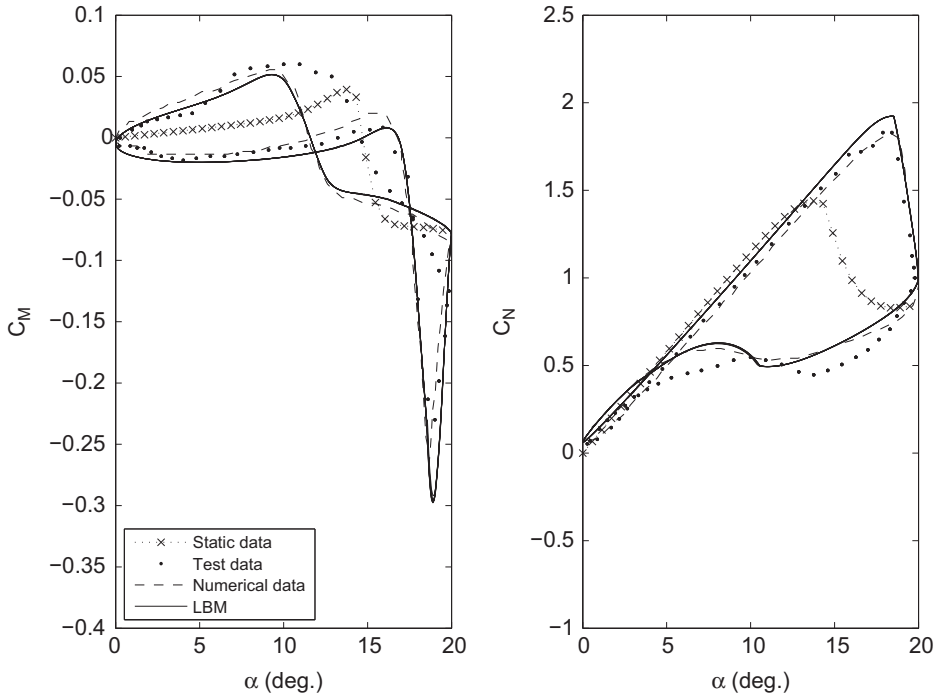


Fig. 3. Verification of the LB model for moderate stall, $\alpha = 10 + 10\sin(0.1S)$ (degrees). The predictions of C_M (left) and C_N (right) using our implementation of the LB model (labelled LBM in the legend) are compared with the experimental data of McCroskey et al. (1976) (Test data) and the numerical results of Leishman and Beddoes (1989) (Numerical data). The static curves of the aerofoil shown here were obtained by McAlister et al. (1983) (Static data).

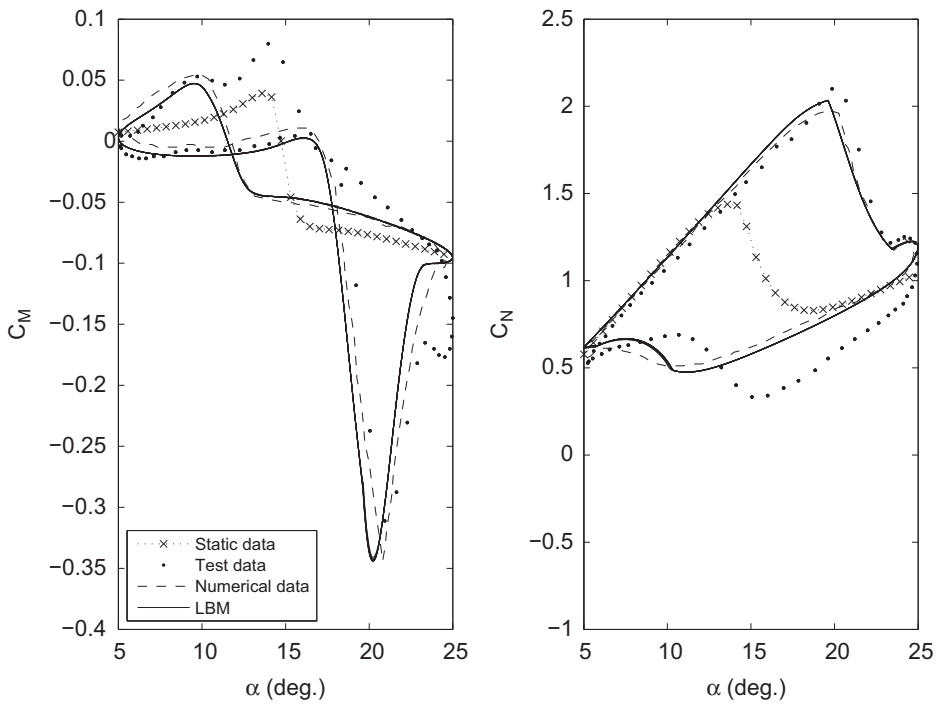


Fig. 4. Verification in the deep stall region, $\alpha = 15 + 10\sin(0.1S)$ (degrees). The entries in the legend are those described in the caption of Fig. 3.

Fig. 4 shows the comparison in the deep stall case. This is a tougher test for the LB model since the increase of the mean angle of incidence by five degrees means that the aerofoil oscillates in and out of stall during the cycle. This case activates all components of the model and constitutes a good test of its ability to model such complex flow. Here the magnitude of the errors calculated using Eq. (21) are $\Delta C_N = 10.2\%$ and $\Delta C_M = 8.4\%$. These errors are significantly

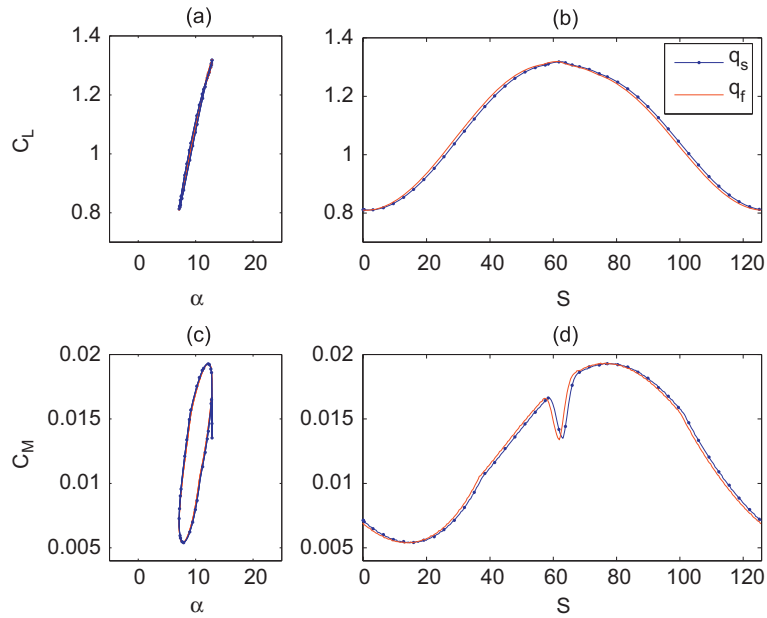


Fig. 5. Forced oscillation given by $\xi = \sin(kS)$, where S denotes the non-dimensional time, with an incidence $\theta = 10^\circ$ and a reduced frequency $k = 0.05$: (a) C_L against the effective angle of incidence α ; (b) time history of C_L ; (c) C_M versus α ; and (d) time history of C_M . The time histories represent a converged cycle of oscillation calculated using the full system (q_f) and the simplified system (q_s).

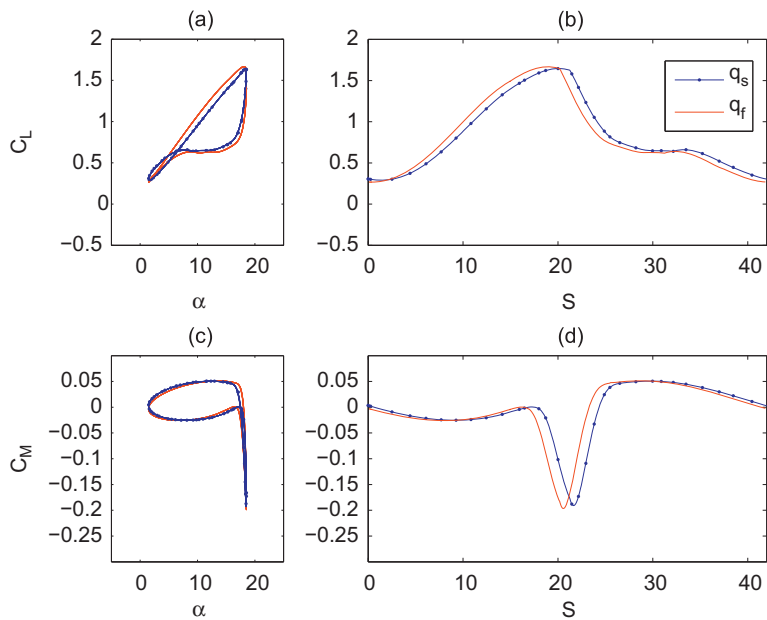


Fig. 6. Forced oscillation given by $\xi = \sin(kS)$ with $\theta = 10^\circ$ and $k = 0.15$: (a) C_L versus α ; (b) time history of C_L ; (c) C_M versus α ; and (d) time history of C_M .

larger than those observed in the case of moderate stall and the largest ones occur again in the reattachment region. This is not surprising since this is the phase of the cycle that is the most difficult to model (Leishman, 2006).

The computed results show that our interpretation of the LB model produces similar values of the aerodynamic coefficients to the original model. In both implementations, the maximum normal force and minimum moment have been found to occur precisely at the same time, which is consistent with the experimental results. The agreement between the LB model and the experimental coefficients is very good, with root-mean square (r.m.s) errors below approximately 10%. The larger discrepancy between computation and experiment is observed during the reattachment period, but this is also present in the original numerical results reported by Leishman and Beddoes (1989).

4. Added mass effects in forced oscillations

We examine the effects that neglecting the added mass terms in the expressions of the effective angle of incidence and pitch rate has on the aerodynamic coefficients of the aerofoil section under forced oscillations in plunge. We consider an aerofoil, at an angle of incidence θ , which oscillates in plunge only with a vertical displacement given by $\zeta = \sin(kS)$, where k denotes the reduced frequency. Simulations using the full and simplified systems were performed over a range of reduced frequencies $0.05 \leq k \leq 0.20$ and angles of incidence $0^\circ \leq \theta \leq 20^\circ$.

The LB model computes the aerodynamic forces at the aerodynamic centre of the aerofoil, hence it requires the effective pitch rate and angle of incidence evaluated there. The aerodynamic centre of the NACA0012 aerofoil is located at the quarter-chord, i.e. $r = a_h + 0.5$. In the following we have taken $a_h = -0.5$ so that $r = 0$ and the elastic and aerodynamic centres coincide. This eliminates the acceleration terms from the effective pitch rate when the aerofoil moves in pitch only. It is also a convenient choice since it will later simplify the calculation of static equilibrium points, namely Eq. (22).

The differences observed between the aerodynamic coefficients C_L and C_M calculated using the full and simplified systems, for an incidence $\theta = 10^\circ$ and a set of frequencies $k = 0.05, 0.15, 0.20$, are shown in Figs. 5, 6 and 7, respectively. This is the typical range of frequencies encountered in helicopter blades (Leishman, 2006).

The results obtained for a reduced frequency $k = 0.05$, depicted in Fig. 5, show very small differences in the aerodynamic coefficients due to the added mass terms. However, at the higher reduced frequencies $k = 0.15$ and 0.20 , shown in Figs. 6 and 7, respectively, the differences become significant. Interestingly, the most significant effect seems to be the presence of a time lag which can be observed in the time evolution of the aerodynamic coefficients.

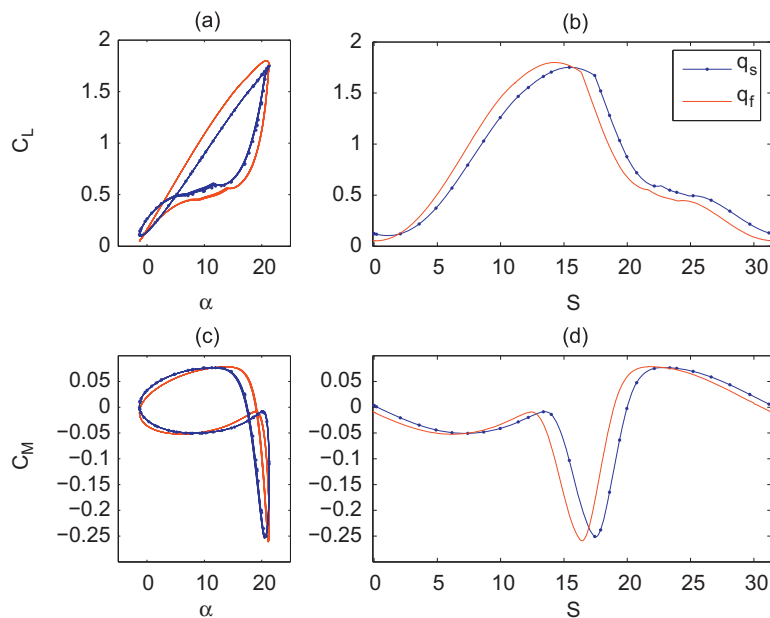


Fig. 7. Forced oscillation given by $\zeta = \sin(kS)$ with $\theta = 10^\circ$ and $k = 0.20$: (a) C_L versus α ; (b) time history of C_L ; (c) C_M versus α ; and (d) time history of C_M .

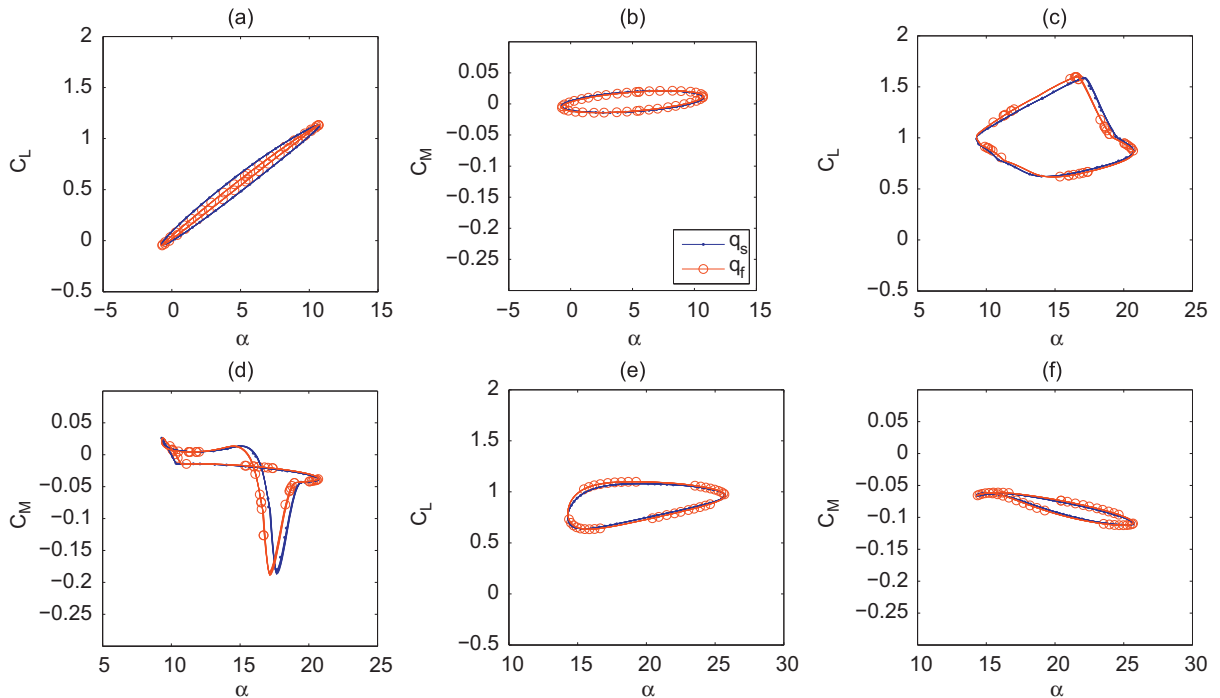


Fig. 8. Plots of C_L and C_M against the effective angle of incidence α for $\xi = \sin(kS)$ and $k = 0.10$ at different fixed geometric angle of incidence θ : (a) and (b) $\theta = 5^\circ$, (c) and (d) $\theta = 15^\circ$, (e) and (f) $\theta = 20^\circ$. The dots and circles represent the solutions obtained with the simplified and full systems, respectively.

The trend in these figures shows that the differences become larger as the reduced frequency increases. This agrees with the findings presented by Hansen et al. (2004). It is also reasonable to expect that an increase in the oscillation frequency would lead to larger values of ζ'' in Eqs. (13) and (14) and therefore the added mass terms will be more significant.

Fig. 8 shows the evolution of the aerodynamic coefficients C_L and C_M for a reduced frequency $k = 0.10$ and a set of angles of incidence $\theta = 5^\circ, 15^\circ, 20^\circ$. The differences observed here between the full and simplified systems are small.

The magnitude of the difference between the curves representing the time evolution of the aerodynamic coefficients calculated using the full and simplified systems will be measured using Eq. (21) with $C_{i_{\max}}$ and $C_{i_{\min}}$; $i = L, M$ taken to be the maximum and minimum values, respectively, of the aerodynamic coefficients during the cycle for the full system.

The calculated values of ΔC_L and ΔC_M for the selected range of reduced frequencies and angles of incidence are shown in Fig. 9. These plots show that errors generated by neglecting the added mass terms increase with the reduced frequency at an approximately constant rate. They also show that the maximum differences are obtained for $\theta = 10^\circ$. This can be explained by the presence of cycles of flow separation and reattachment in the range $10^\circ \leq \theta \leq 15^\circ$ which are not present elsewhere.

We therefore conclude that in the range of frequencies considered here ($0.05 \leq k \leq 0.2$), disregarding the added mass terms in forced oscillations leads mostly to phase errors that increase linearly with the reduced frequency, but these errors are of the same order of magnitude as the errors observed when comparing the computational results of the LB model with the experimental data in Section 3. However, it should be noted that the choice of $r = 0$ here eliminates some of the added mass terms so we would expect the effect of neglecting the added mass terms to be larger in cases with more complex kinematics, for instance when $r \neq 0$ and when the flows are highly unsteady ($k > 0.2$).

5. Added mass effects in free oscillations

Here we use a linear stability analysis to determine the range of parameters of the aeroelastic system where neglecting added mass effects leads to significant differences in the location of the flutter boundaries. Flutter instability is the common name used in aeroelasticity to refer to a Hopf bifurcation where there is a transition (in the phase space) from

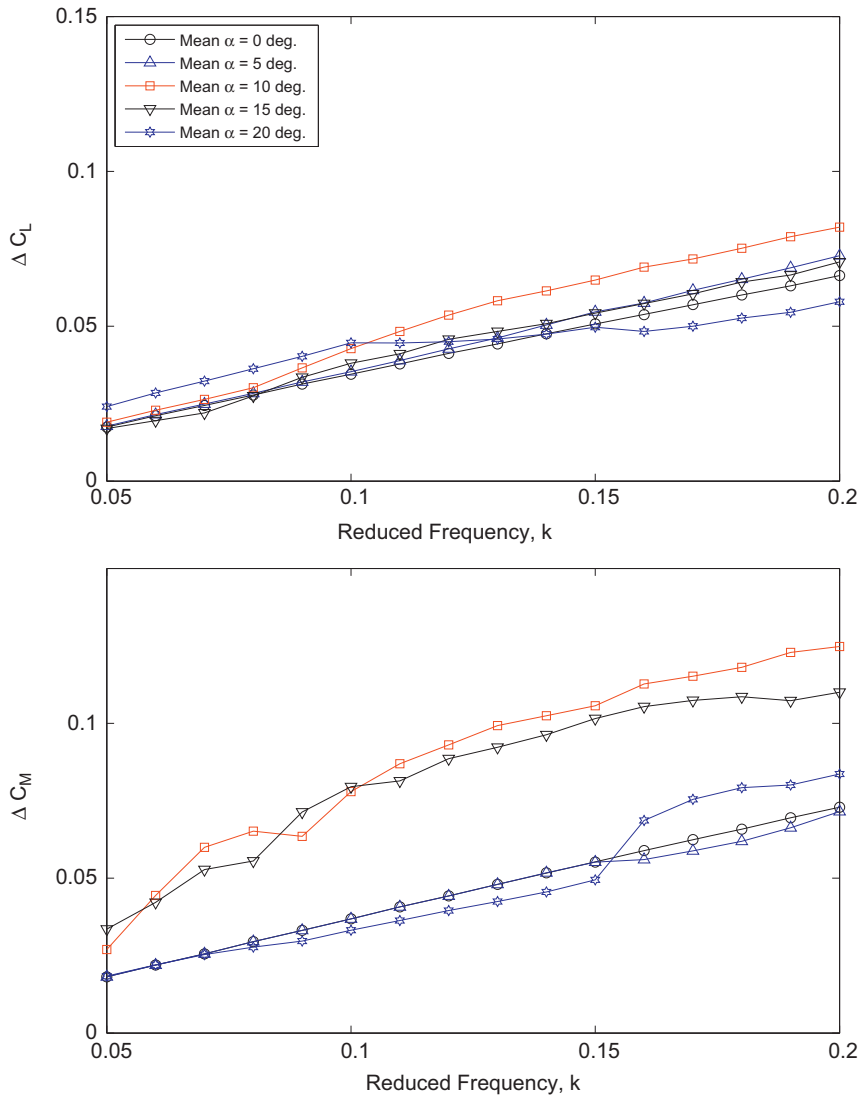


Fig. 9. Plots of ΔC_L and ΔC_M for a range of reduced frequencies $0.05 \leq k \leq 0.20$ and a range of mean angles of incidence $0^\circ \leq \theta \leq 20^\circ$.

a fixed point to a limit cycle oscillation. The value of the parameter for which the bifurcation occurs is called a bifurcation point (in parameter space) or critical value.

In the aeroelastic system, a fixed point represents a position of the airfoil where the aerodynamic lift and pitching moment are in equilibrium with the restoring forces exerted by the springs. The fixed point is the solution of a *static* equilibrium problem. Under a static condition, the LB model simplifies to Kirchhoff's theory, as described for instance by Leishman (2006), which involves only the incidence angle θ .

To allow the fixed point to move through different regions of the aeroelastic system separated by the *discontinuity boundaries* of the LB model (see Fig. 11), we follow the approach proposed by Tang and Dowell (1996) and introduce a new parameter, the *spring offset angle* θ_0 . The role of this angle is to achieve static equilibrium between aerodynamic loads and structural response over a range of angles of incidence. The static equilibrium angle of incidence θ (which corresponds to x_{13} in the LB model) is the solution of the uncoupled nondimensional equation of motion in rotation given by

$$\frac{\mu \pi r_\alpha^2}{2U^*2} (\theta - \theta_0) = \frac{(\frac{1}{2} + a_h)}{2} C_N(\theta) + C_M(\theta). \quad (22)$$

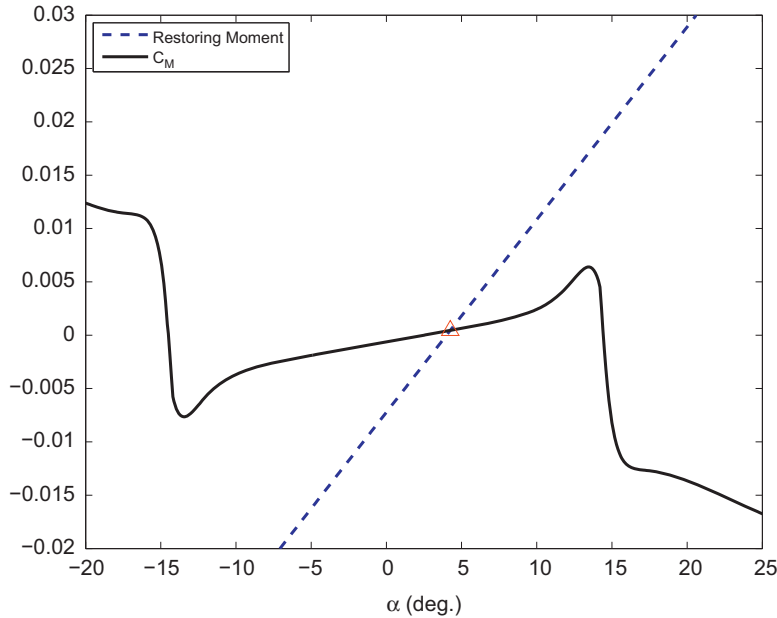


Fig. 10. Solution of the static equilibrium equation in rotation (22) with $a_h = -\frac{1}{2}$.

This equation is obtained by considering a stationary point of Eq. (2) which has been suitably modified to incorporate a torsional spring with zero restoring moment at angle of incidence $\theta = \theta_0$. We will use $a_h = -\frac{1}{2}$ so the solution is the intersection between the pitching moment curve and the spring restoring moment as illustrated in Fig. 10. The remaining states of the fixed points can be found by substituting the solution of Eq. (22) into the uncoupled translation equation of motion and the state-space LB model.

The equilibrium point changes its position when one of the parameters of the system is altered. Here, four parameters will be considered: θ_0 , M , $\bar{\omega}$ and μ . Given that $\mathbf{x}' = \mathbf{0}$, the fixed points of the full and simplified aeroelastic systems coincide since $\mathbf{f}_f(\mathbf{x}, \mathbf{0}) = \mathbf{f}_s(\mathbf{x}) = \mathbf{0}$.

Discontinuities exist in the phase space of the aeroelastic system because of the piecewise definition of the LB model at $x_9 = \pm C_{N1}$ and $x_{13} = \pm \alpha_1$. Here C_{N1} denotes a critical value of C_N above which, if x_9 is increasing, a vortex is shed from the leading edge, and α_1 corresponds to the aerofoil static stall angle of incidence. The LB model uses $x_9 = \pm C_{N1}$ as a switch to indicate the shedding of the leading edge vortex which affects the values of time parameters in the state-space LB model ODEs. Hence, $x_9 = \pm C_{N1}$ represents a discontinuity boundary in the phase space of the aeroelastic system.

The dynamic trailing edge separation point x_{10} is a nonsmooth function of x_{13} and α_1 . The discontinuity is located at $x_{10} = 0.70$ which corresponds to $x_{13} = \alpha_1$. However, α_1 is a variable parameter whose value depends on the flow condition around the airfoil. It is therefore convenient to make α_1 a constant for a given Mach number so that the discontinuity described by $x_{13} = \alpha_1$ can be drawn as a line in Fig. 11.

There are several other discontinuities in the LB model which affect the dynamics of the system, but they can safely be ignored when the fixed point is not close to the discontinuity since only small perturbations about the fixed points are of interest here. A complete description of the discontinuities in this implementation of the LB model is given by Chantharasenawong (2007).

Fig. 11 shows the regions in the $\theta_0 - M$ and $\bar{\omega} - \mu$ planes delimited by the $x_9 = C_{N1}$ and $x_{13} = \alpha_1$ discontinuities. In Fig. 11(a) the out-of-plane parameters are fixed at $\bar{\omega} = 0.80$ and $\mu = 100$, while $\theta_0 = 10^\circ$ and $M = 0.30$ in Fig. 11(b). The two planes represent the four-dimensional parameter space with the crosses indicating the only point common to both planes. The discontinuities partition the area shown in the figure into three separate regions which are characterised by:

- (i) Region 1: $x_9 < C_{N1}$ and $x_{13} < \alpha_1$. This is the linear flutter region where no discontinuity associated with dynamic stall has been triggered.
- (ii) Region 2: $x_9 > C_{N1}$ and $x_{13} < \alpha_1$. In this intermediate stall region, the leading edge vortex has started but the geometric angle of incidence is still below the static stall angle.

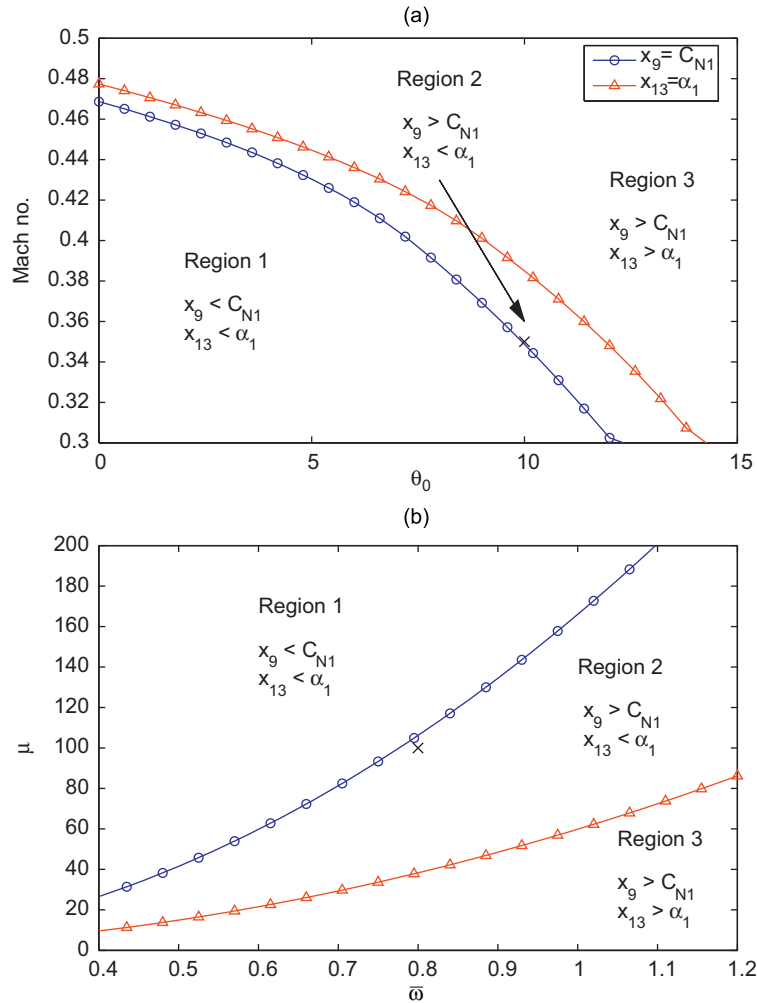


Fig. 11. Plots of regions in the parameter space delimited by $x_9 = C_{N1}$ and $x_{13} = \alpha_1$ discontinuity boundaries on (a) $\theta_0 - M$ plane and (b) $\bar{\omega} - \mu$ plane. Each region relates to the x_9 and x_{13} coordinates of the fixed point. The crosses in the figures indicate the point where $\theta_0 = 10^\circ$, $M = 0.35$, $\bar{\omega} = 0.80$ and $\mu = 100$.

- (iii) Region 3: $x_9 > C_{N1}$ and $x_{13} > \alpha_1$. This is the stall flutter region where all dynamic stall discontinuities are activated. It is sometimes referred to as the deep stall region.

Fig. 11 shows that varying the parameters of the system ($\theta_0, M, \bar{\omega}, \mu$), the fixed point can move through several regions where the Jacobian matrices of the right-hand side terms of the systems (15) and (20) are defined differently. The investigation that follows will choose three points (one in each region) in the parameter space away from the discontinuities to study the effect of neglecting the added mass terms.

The method used to generate Fig. 11(a) is the following. We fix two of the parameters, namely $\bar{\omega} = 0.80$ and $\mu = 100$, and vary the spring offset angle θ_0 between 0 and 15 and the Mach number M between 0.3 and 0.5. The value of M for which $x_9 = C_{N1}$, where x_9 is the coordinate of the fixed point, is marked by a circle. Similarly, a triangle represents the condition $x_{13} = \alpha_1$. The same method has been applied to produce Fig. 11(b) where M and θ_0 are fixed instead.

To determine the behaviour of the system in each of the three regions, the calculation of the Hopf bifurcation point at three different locations in the parameter space will be examined in Section 5.3. The behaviour of the system at the two discontinuity boundaries would also be of interest. However, a bifurcation along such boundaries is not generic. Here we will deal only with the generic cases and leave the non-generic ones for future research.

5.1. Calculation of the Hopf bifurcation points

The Hopf bifurcation is a bifurcation in which a stable fixed point of a dynamical system loses its stability as a conjugate pair of eigenvalues of the linearised system crosses the imaginary axis of the complex plane. The stability of the linear system relates to the stability of the nonlinear system (Guckenheimer and Holmes, 2002). An infinitesimal amplitude limit cycle oscillation motion is expected to be created at the Hopf bifurcation as the stable fixed point changes its stability.

The linear stability of a fixed point of the full aeroelastic system (15), away from discontinuities in this right-hand side term, can be analysed by introducing a perturbation vector $\delta \mathbf{x}$ to the state variables representing a generic point \mathbf{x} of the aeroelastic system leading to the system of ODEs

$$\mathbf{x}' + \delta \mathbf{x}' = \mathbf{f}_f(\mathbf{x} + \delta \mathbf{x}, \mathbf{x}' + \delta \mathbf{x}').$$

The right-hand side can be expanded in a truncated Taylor series to read

$$\mathbf{x}' + \delta \mathbf{x}' = \mathbf{f}_f(\mathbf{x}, \mathbf{x}') + \left. \frac{\partial \mathbf{f}_f}{\partial \mathbf{x}} \right|_{(\mathbf{x}, \mathbf{x}')} \delta \mathbf{x} + \left. \frac{\partial \mathbf{f}_f}{\partial \mathbf{x}'} \right|_{(\mathbf{x}, \mathbf{x}')} \delta \mathbf{x}'$$

and, given that Eq. (15) is satisfied, the expression is simplified to the evolution equation of the small perturbations to the system at $(\mathbf{x}, \mathbf{x}')$

$$\delta \mathbf{x}' = \left[\left(\mathbf{I} - \left. \frac{\partial \mathbf{f}_f}{\partial \mathbf{x}'} \right|_{(\mathbf{x}, \mathbf{x}')} \right)^{-1} \left. \frac{\partial \mathbf{f}_f}{\partial \mathbf{x}} \right|_{(\mathbf{x}, \mathbf{x}')} \right] \delta \mathbf{x} = \mathbf{J}_f \delta \mathbf{x},$$

where \mathbf{J}_f denotes the Jacobian matrix of the full aeroelastic system (15). Its eigenvalues λ_f will determine the stability of the full aeroelastic system. For a fixed point we will have $\mathbf{x}' = \mathbf{0}$ and, if it is a Hopf bifurcation, a conjugate pair of eigenvalues will simultaneously cross the imaginary axis, i.e. there will be two eigenvalues of the form $\lambda_{f_{1,2}} = \pm \vartheta i$, where ϑ is a real number and $i = \sqrt{-1}$.

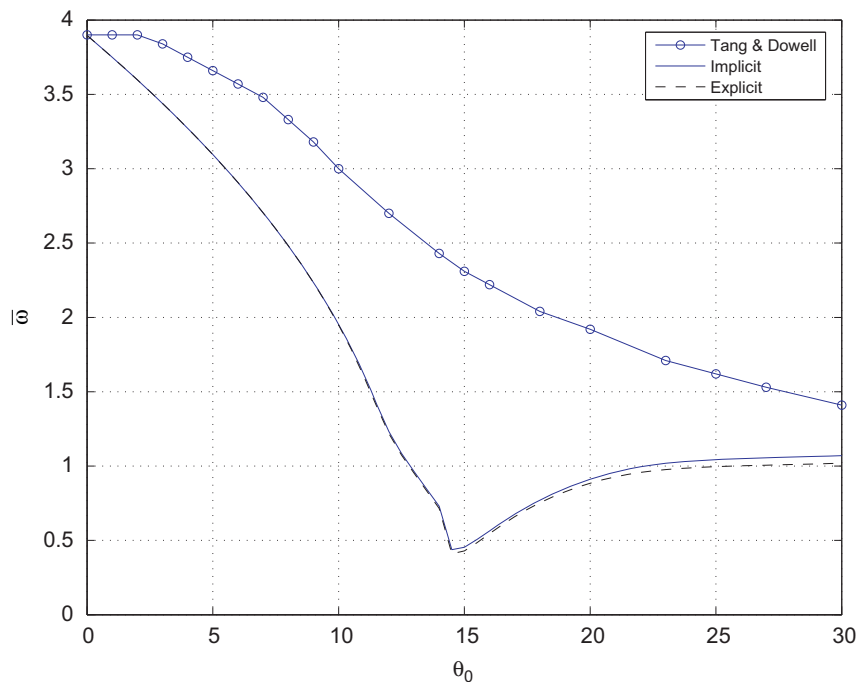


Fig. 12. Flutter boundary for $\bar{\omega}$ as a function of the spring offset angle θ_0 : comparison of the values obtained with the implicit and explicit systems based on the LB model and those reported by Tang and Dowell (1996) using the ONERA model.

The simplified system that results from neglecting the added mass terms is given by Eq. (20) and a similar derivation leads to an evolution equation for small perturbations of the form

$$\delta \mathbf{x}' = \mathbf{J}_s \delta \mathbf{x} = \left. \frac{\partial \mathbf{f}_s}{\partial \mathbf{x}} \right|_{\mathbf{x}} \delta \mathbf{x},$$

where \mathbf{J}_s denotes the Jacobian matrix of the simplified aeroelastic system (20) and its eigenvalues again determine the stability of the system.

5.2. Comparison with the ONERA model

The methodology described in the previous section can be applied to the calculation of flutter boundaries as the loci of the Hopf bifurcation points of the system. In the absence of suitable experimental data to validate our approach, we compare the calculation of the flutter boundary for $\bar{\omega}$ (or alternatively the reduced velocity) as a function of the spring offset angle θ_0 with the results obtained by Tang and Dowell (1996) using the ONERA model.

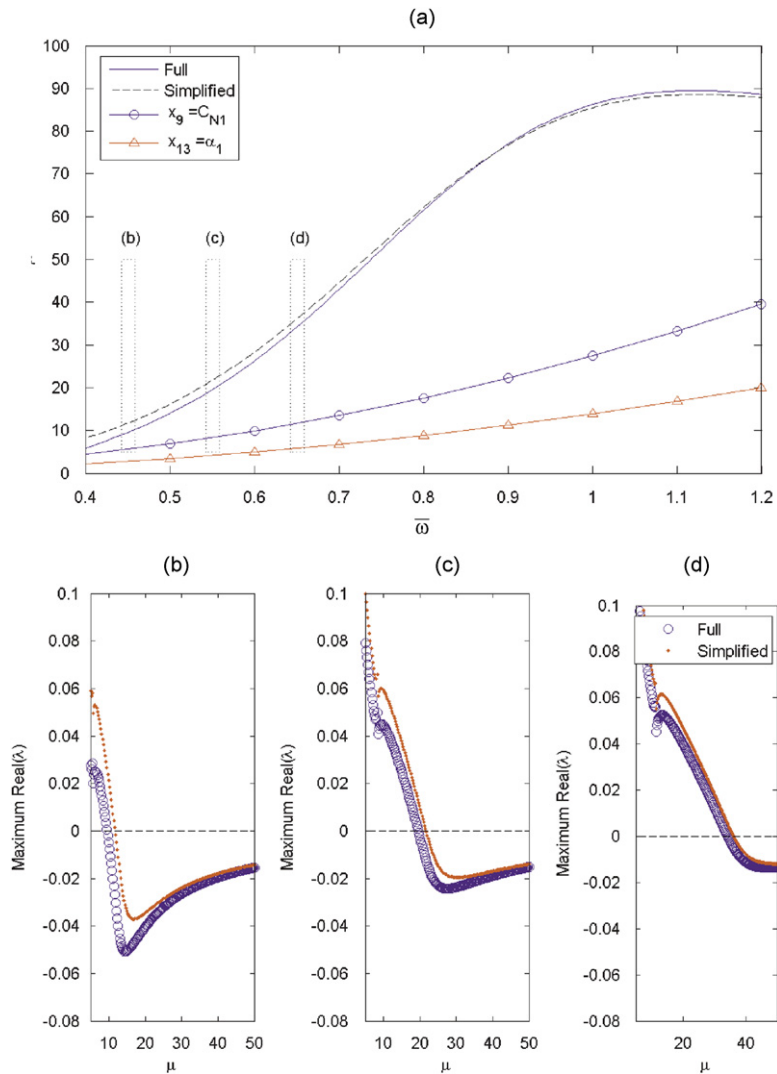


Fig. 13. (a) Plots of Hopf bifurcation curves in region 1 and the discontinuity boundaries in the $\bar{\omega}$ - μ plane ($M = 0.3, \theta_0 = 10^\circ$). Figures (b)–(d) show plots of the maximum real parts of the eigenvalues in the range $5 \leq \mu \leq 50$ at $\bar{\omega} = 0.45, 0.55$ and 0.65 , respectively.

The aerodynamic and structural characteristics of the aerofoil section have been chosen so that the flutter values for $\theta_0 = 0$ of both dynamic stall models coincide. The values obtained with the implicit and explicit systems based on the LB model are compared with those obtained using the ONERA model in Fig. 12.

The LB model consistently predicts, over the range of θ_0 considered here, a flutter value of $\bar{\omega}$ lower than that obtained with the ONERA model. Both methods show a reduction of the flutter value of $\bar{\omega}$ as the spring offset angle increases for values of $\theta_0 < 15^\circ$. For values of θ_0 above this value, the two models behave in opposite ways with the LB model predicting an increase of the critical value of $\bar{\omega}$ with θ_0 . This is not surprising since the modelling of stall behaviour is very different in both models.

The flutter boundary curve obtained with the ONERA model is a continuous function of θ_0 . The curve calculated using the LB model presents a discontinuity of slope at $\theta_0 \approx 15^\circ$. This is a consequence of the piecewise smooth definition of the LB model which has been shown to affect significantly the dynamical behaviour of the aeroelastic system in Galvanetto et al. (2008).

Focusing on the prediction by the LB model only, it can be seen that the discrepancies due to the added mass terms are larger as θ_0 increases towards the deep stall region. This will be analysed in more detail in the next section.

This comparison cannot be considered a validation of the evaluation of flutter boundaries by the LB model, but it shows that the use of the LB model results in similar trends and orders of magnitude of the critical values to those calculated with the well-established ONERA dynamic stall model. It also highlights that dynamic stall models, even if their parameters have been optimized for a particular aerofoil, could produce results that differ significantly. More importantly, the magnitude of the differences is considerably larger than the errors observed in predicting the experimental values of the aerodynamic coefficients of the aerofoil.

5.3. Assessment of added mass effects

The analysis of the effect of neglecting the added mass terms on the calculation of flutter boundaries will be performed over a range of $\bar{\omega}$ at fixed values of Mach number and θ_0 , i.e. in the $\bar{\omega}-\mu$ plane similar to Fig. 11(b). The reason for not using the θ_0-M plane is because the parameters C_{N1} and α_1 are functions of the Mach number, and this can make the presentation of these results in that plane confusing.

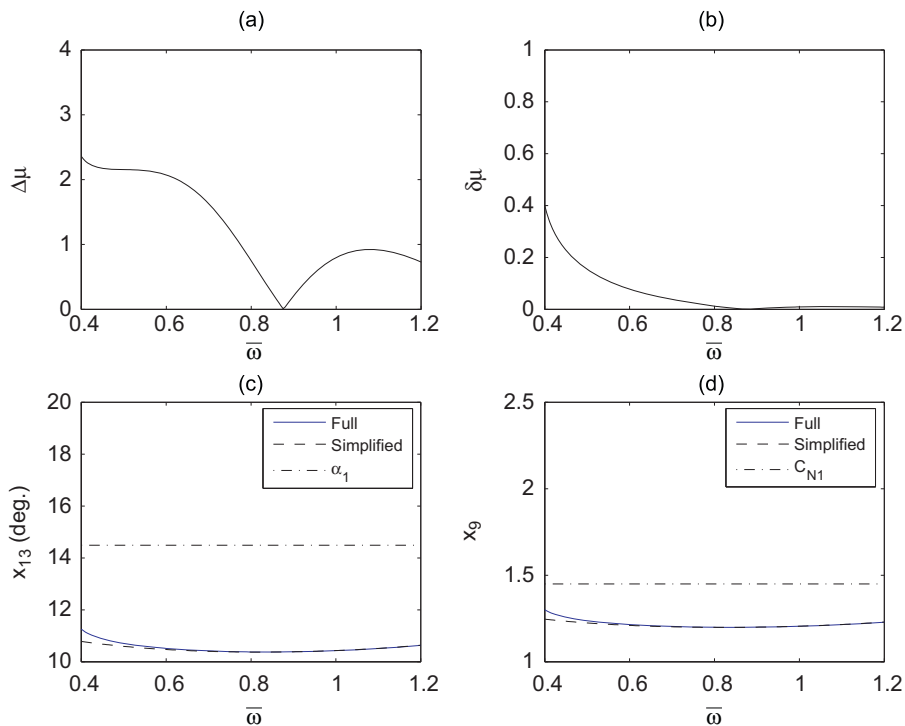


Fig. 14. Characteristics of the Hopf bifurcation in region 1: (a) absolute difference $\Delta\mu$, (b) relative difference $\delta\mu$, (c) x_{13} along Hopf bifurcation curves, (d) x_9 along Hopf bifurcation curves.

Recall that the aeroelastic system is partitioned by the discontinuity boundaries into three separate regions as illustrated in Fig. 11. The analysis here will involve finding the Hopf bifurcation in these regions. Three cases will be considered:

- (1) Hopf bifurcation in region 1 ($x_{13} < \alpha_1$ and $x_9 < C_{N1}$);
- (2) Hopf bifurcation in region 2 ($x_{13} < \alpha_1$ and $x_9 > C_{N1}$);
- (3) Hopf bifurcation in region 3 ($x_{13} > \alpha_1$ and $x_9 > C_{N1}$).

In the following analysis the symbols \mathbf{J}_k^1 , \mathbf{J}_k^2 and \mathbf{J}_k^3 , where $k = f$ or s , will denote the Jacobian matrices of the full or simplified aeroelastic system in regions 1–3, respectively.

5.3.1. Case 1: Hopf bifurcation in region 1

This region may be referred to as the linear region because it is associated with small values of angle of incidence and the highly nonlinear components of the LB model are not activated. This calculation is effectively a classical flutter analysis.

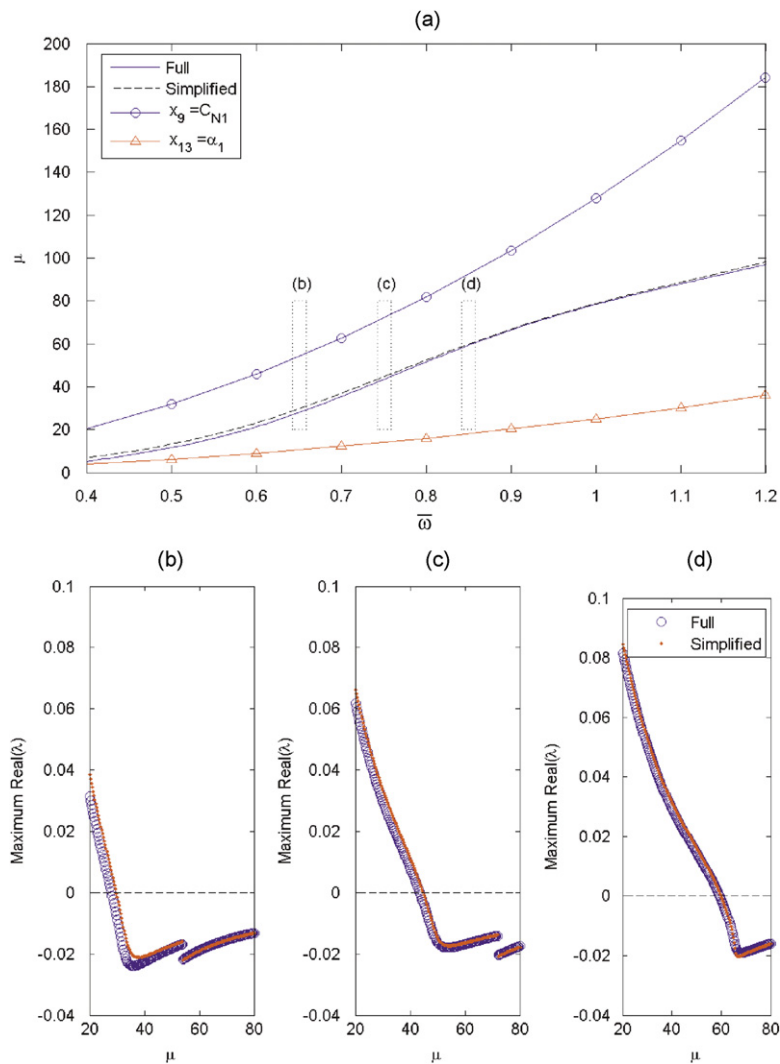


Fig. 15. (a) Plots of Hopf bifurcation curves in region 2 and the discontinuity boundaries in the $\bar{w}-\mu$ plane ($M = 0.3, \theta_0 = 12^\circ$). Figures (b)–(d) show plots of the maximum real parts of the eigenvalues in the range $20 \leq \mu \leq 80$ at $\bar{w} = 0.65, 0.75$ and 0.85 , respectively.

The Hopf bifurcation curves of the full and simplified aeroelastic systems and the discontinuity boundaries are shown in Fig. 13(a). This $\bar{\omega}-\mu$ plane is characterised by $\theta_0 = 10^\circ$ and $M = 0.30$. The Hopf bifurcation curves lie in region 1 for $0.40 \leq \bar{\omega} \leq 1.20$. Despite the small difference in numerical values, the Hopf bifurcation curves for both systems behave similarly in the given range of $\bar{\omega}$.

Figs. 13(b)–(d) show the variation in the maximum real parts of the eigenvalues at different values of $\bar{\omega}$. The range of μ used in Figs. 13(b)–(d) are indicated by the corresponding boxes in Fig. 13(a). The maximum real parts shown in these figures are shared by a pair of eigenvalues, which confirms that the Hopf bifurcation has occurred. In Figs. 13(b)–(d), jumps are observed in the plots of eigenvalues at low values of μ .

The differences between the full and simplified aeroelastic systems can be characterised by

$$\Delta\mu = |\mu_f - \mu_s|, \quad \delta\mu = \frac{\Delta\mu}{\mu_f}, \tag{23}$$

where μ_f and μ_s are the values of the mass ratio μ at the Hopf bifurcation in the full and simplified aeroelastic system, respectively. The differences between the Hopf bifurcation curves are presented in Figs. 14(a) and (b). The maximum value of $\Delta\mu$ is observed at $\bar{\omega} = 0.40$ and its value reaches zero at $\bar{\omega} \approx 0.85$ which indicates the intersection of full and simplified Hopf bifurcation curves. The maximum relative difference of $\delta\mu = 0.40$ is observed at $\bar{\omega} = 0.40$. This is because $\delta\mu$ is amplified by the small values of μ even though the absolute difference $\Delta\mu$ is not significantly large. It is the opposite when $\bar{\omega} > 0.80$ where $\delta\mu$ is almost negligible.

Figs. 14(c) and (d) show the variations of x_{13} and x_9 at the Hopf bifurcation for the same range of $\bar{\omega}$. The plots show that both variables are below their respective critical values, in agreement with the linear characteristics of region 1. The differences between the full and simplified systems in this region are large when the values of μ at the Hopf bifurcation are low. This implies that the acceleration terms could have significant effects on aeroelastic systems operating at low values of μ or $\bar{\omega}$, and their contributions should not be neglected from the modelling. This is in accordance with the well-known result of linear aeroelastic theory for small oscillations, but even though we are considering linear aerodynamics, i.e. the aerodynamic coefficients are proportional to α and q , these are non-linear functions of the geometry here.

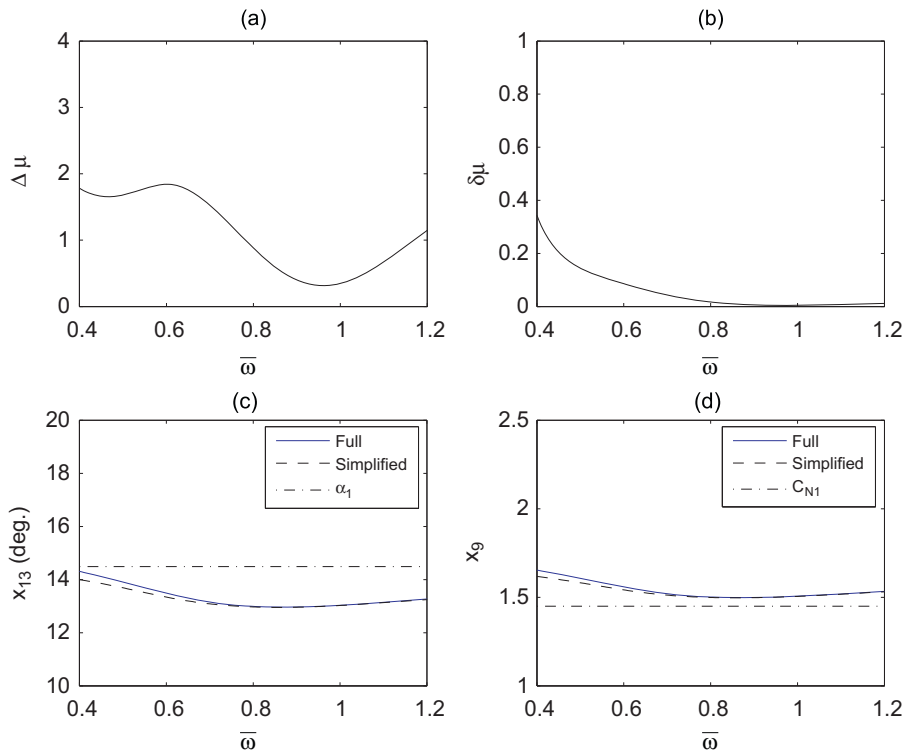


Fig. 16. Characteristics of the Hopf bifurcation in region 2: (a) absolute difference $\Delta\mu$, (b) relative difference $\delta\mu$, (c) x_{13} along Hopf bifurcation curves, (d) x_9 along Hopf bifurcation curves.

5.3.2. Case 2: Hopf bifurcation in region 2

This region is bounded by the two discontinuity boundaries and is the smallest in area when compared to other regions. This significantly narrows down the range of parameters θ_0 and M for which the Hopf bifurcation curves in the $\bar{\omega}-\mu$ plane lie in region 2. The plots presented in this section are obtained by using $\theta_0 = 12^\circ$ and $M = 0.30$.

Fig. 15 shows that the Hopf bifurcation curves lie between the two discontinuity boundaries in the $\bar{\omega}-\mu$ plane. The value of μ is small at the Hopf bifurcation at low values $\bar{\omega}$, and it increases as $\bar{\omega}$ grows. The shape of the curves is also similar to that observed in region 1. This can be explained by the fact that the components of the Jacobian matrices \mathbf{J}^1 and \mathbf{J}^2 have the same expressions but with different values of the time parameters T_f and T_v (see Appendix A).

The variation of the maximum real parts of the eigenvalues at three sample values of $\bar{\omega}$ are shown in Figs. 15(b)–(d). These points represent a conjugate pair of eigenvalues that have changed sign, so these figures represent the Hopf bifurcation. The behaviour of $\Delta\mu$ and $\delta\mu$ shown in Figs. 16(a) and (b), respectively, is similar to that observed in region 1. The value of $\Delta\mu$ fluctuates between 0.50 and 1.90 and its minimum occurs at $\bar{\omega} \approx 0.95$. The relative difference $\delta\mu$ is amplified by the low values of μ when $\bar{\omega}$ is small. The maximum value of $\delta\mu$ is approximately 0.30 and it corresponds to $\bar{\omega} = 0.40$. The difference between the full and simplified systems in region 2 is large when $\bar{\omega} < 0.80$. This behaviour is similar to that observed in region 1 because the expressions of the Jacobian matrices \mathbf{J}_k^1 and \mathbf{J}_k^2 are the same and the only

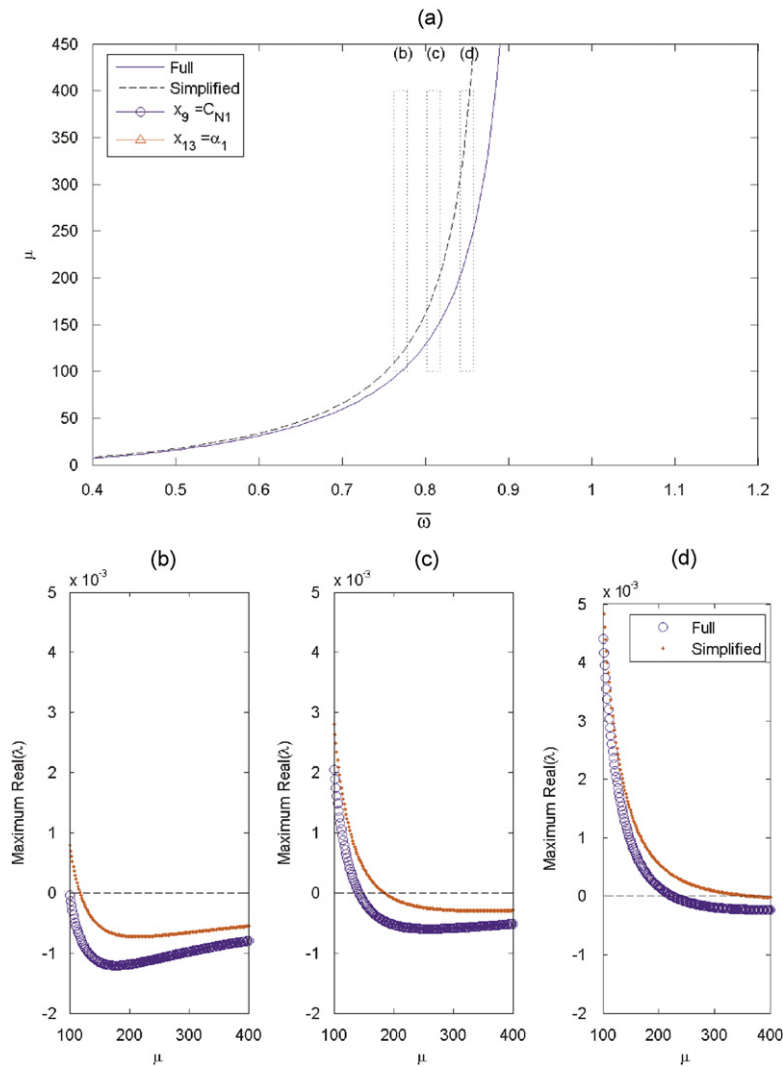


Fig. 17. (a) Plots of Hopf bifurcation curves in region 3 in the $\bar{\omega}-\mu$ plane ($M = 0.3$, $\theta_0 = 18^\circ$). Figures (b)–(d) show plots of the maximum real parts of the eigenvalues in the range $100 \leq \mu \leq 400$ at $\bar{\omega} = 0.77$, 0.81 and 0.85, respectively.

difference is due to some minor changes in the values of the time constants T_f and T_b . Figs. 16(c) and (d) show the coordinates x_{13} and x_9 of the fixed points at the Hopf bifurcation curves, and confirm that they lie in region 2.

5.3.3. Case 3: Hopf bifurcation in region 3

Region 3 may be referred to as the stall region because all non-linear components of the LB model are active here. The fixed points in this region are characterised by $x_{13} > \alpha_1$ and $x_9 > C_{N1}$. These correspond to a large angle of incidence. The results presented in this section are obtained by using $\theta_0 = 18^\circ$ and $M = 0.30$.

Fig. 17(a) shows only the Hopf bifurcation curves in the parameter plane. The discontinuity boundaries are not shown here because they are outside the range of μ used in the calculations ($1 \leq \mu \leq 5000$), however, only values $0 \leq \mu \leq 450$ are shown in the figure. Nonetheless, Figs. 18(c) and (d) provide evidence that the Hopf bifurcation curves lie in region 3. The maximum real parts of the eigenvalues at three sampling values of $\bar{\omega}$ are shown in Figs. 17(b)–(d). Unlike in regions 1 and 2, the eigenvalues of the two systems are clearly apart from each other, showing a distinct shift in the Hopf bifurcation.

The absolute difference $\Delta\mu$ increases with $\bar{\omega}$ up to $\bar{\omega} \approx 0.90$ where it experiences a very rapid growth as shown in Fig. 18. The relative difference $\delta\mu$ is now at its maximum when $\bar{\omega}$ is large, which is opposite to the behaviour shown in cases 1 and 2. This is due to the change in the expressions of the Jacobian matrix when the fixed point crosses the $x_{13} = \alpha_1$ discontinuity boundary. The minimum value of $\Delta\mu$ is found at $\bar{\omega} = 0.40$ while that of $\delta\mu$ is found at $\bar{\omega} = 0.60$. An increase in $\delta\mu$ toward the low values of $\bar{\omega}$ shown in Fig. 18(b) is due to the small values of μ at the Hopf bifurcation which act as the denominator for the relative difference.

In this region, which represents highly separated flows ($x_{13} > \alpha_1$), the effect of the added mass terms is significant when the Hopf bifurcation occurs at high values of μ . This is opposite to the findings in region 1, the linear region.

The Hopf bifurcation points calculated with the eigenanalysis have also been obtained through numerical integration and shown to agree by Chantharasenawong (2007).

The Jacobian matrices of the full and simplified aeroelastic systems have the same fixed points, as both systems reduce to the same system of algebraic equations for $\mathbf{x}' = \mathbf{0}$, but their eigenvalues are different and, as a result, neglecting the acceleration terms results in a shift of the Hopf bifurcation. The shift in the Hopf bifurcations in μ is illustrated by plotting the Hopf bifurcation curves in a two-parameter plane, as shown in Fig. 19. The shift is

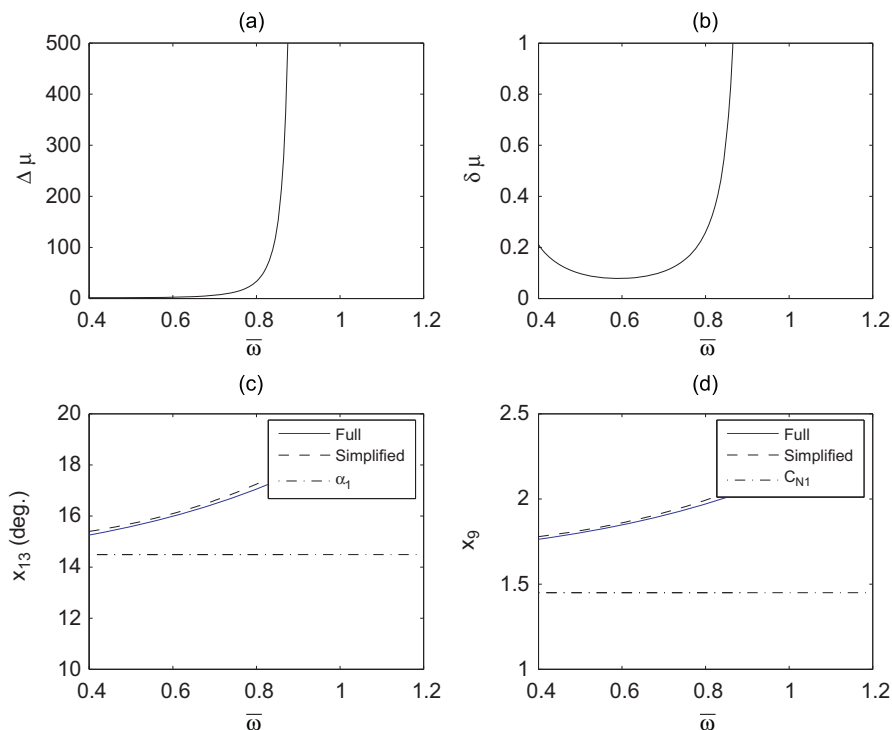


Fig. 18. Characteristics of the Hopf bifurcation in region 3: (a) absolute difference $\Delta\mu$, (b) relative difference $\delta\mu$, (c) x_{13} along Hopf bifurcation curves, (d) x_9 along Hopf bifurcation curves.

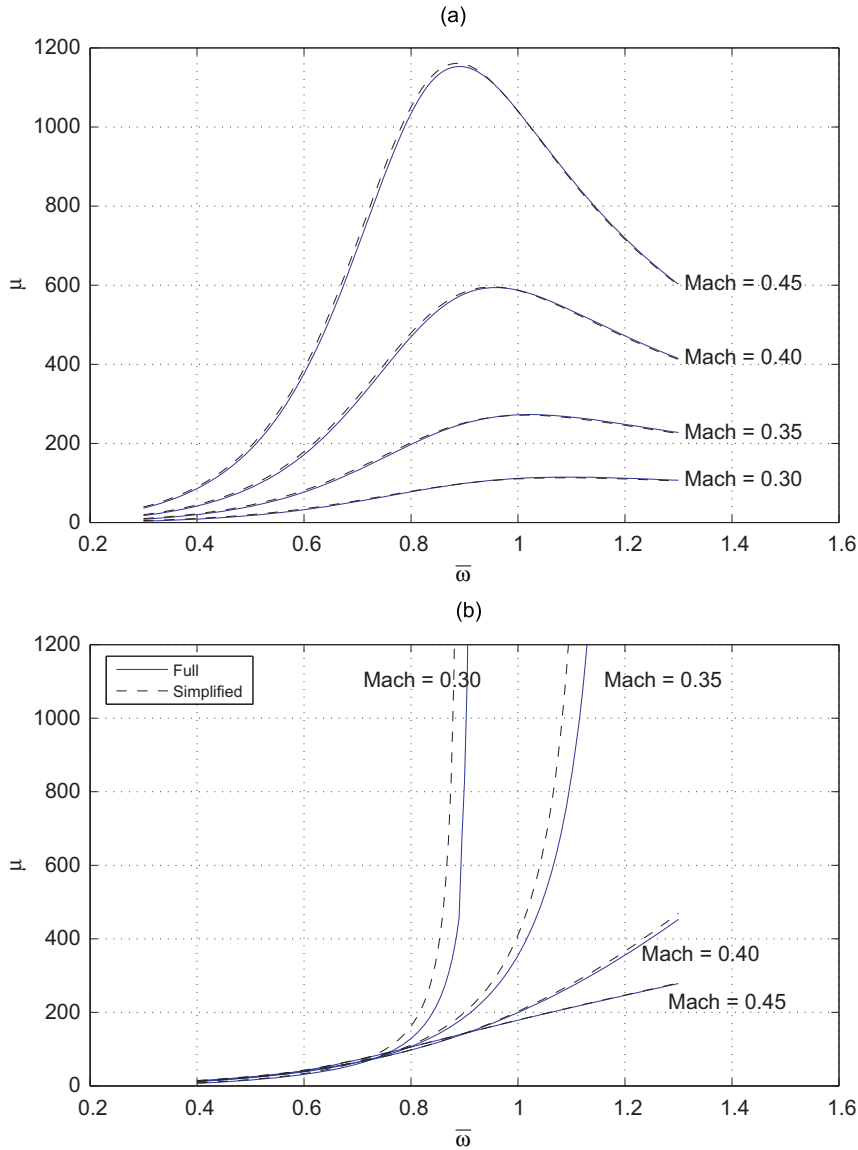


Fig. 19. Hopf bifurcation curves on the $\bar{\omega}$ - μ plane in the range $0.35 \leq M \leq 0.45$ in (a) region 1 ($\theta_0 = 4^\circ$) and (b) region 3 ($\theta_0 = 18^\circ$).

represented by the gap between the two Hopf bifurcation curves generated at the same Mach number. Because of the small size of region 2, the curves often intersect with the discontinuity boundaries that border it, hence they are not shown in this figure.

5.4. Effect of added mass terms on $\Delta\mu$ and $\delta\mu$

The shift or difference in the Hopf bifurcations in μ is measured by $\Delta\mu$ and the relative difference by $\delta\mu$. These act as indicators of the magnitude of the effects of the acceleration terms.

Fig. 20 shows plots for $\delta\mu$ of the Hopf bifurcation curves in Fig. 19. With $\theta_0 = 4^\circ$, Fig. 20(a) represents the behaviour of the differences in region 1 of the aeroelastic system parameter space. The maximum $\delta\mu$ is observed at low values of $\bar{\omega}$. This can be explained by the small values of μ at the Hopf bifurcation compared to $\Delta\mu$. Fig. 20(b) shows a similar plot for the system in region 3 of the parameter space. The maximum values of $\delta\mu$ are sometimes greater than unity and are found at large values of $\bar{\omega}$ instead. It means that the effects of the acceleration terms are significant at low mass ratios in

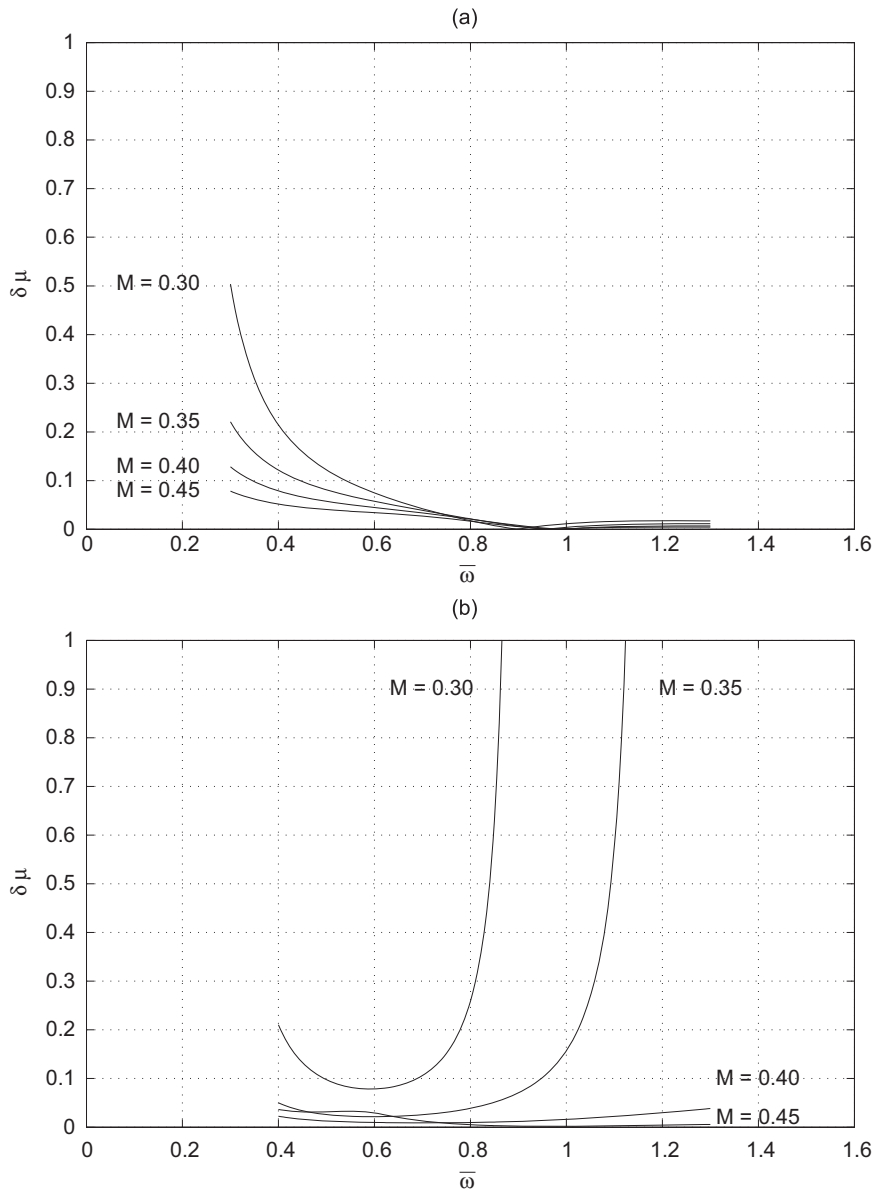


Fig. 20. Relative differences between Hopf bifurcation curves in the range $0.35 \leq M \leq 0.45$ in (a) region 1 ($\theta_0 = 4^\circ$) and (b) region 3 ($\theta_0 = 18^\circ$).

the linear aerodynamic region and at high mass ratios in the stall region. In these cases, the aerodynamic system must be described by a system of implicit ODEs and an appropriate numerical integration has to be used.

6. Conclusions

We have investigated the importance of added mass terms in the dynamics of a typical airfoil section, both in forced and free oscillations.

In the case of forced oscillations, the results show that neglecting the added mass terms introduces a time lag or shift in the time history of the aerodynamic coefficients that increases with the reduced frequency but has a very small effect in their amplitude. The r.m.s. errors that this originates increase at a constant rate with increases of the reduced

frequency. However, the errors observed in the range $0.05 \leq k \leq 0.2$ are always below 15% and their magnitude is comparable to that of the errors incurred in matching the experimental data.

In free oscillations, we investigated the effects of the added mass terms in calculating the flutter boundaries at small ($\theta_0 = 4^\circ$) and large ($\theta_0 = 18^\circ$) values of the spring offset angle for the range of frequencies ratio $0 < \bar{\omega} < 1.4$. The results show that for low values of the spring offset angle, these terms should be included for low values of the mass ratio, or the ratio of natural frequencies, at low incidences. For high values of the spring offset angle, corresponding to stall flutter, the terms are important for large values of the mass ratio. They also show that the maximum differences are obtained for $\theta = 10^\circ$. This can be explained by the presence of cycles of flow separation and reattachment in the range $10^\circ \leq \theta \leq 15^\circ$ which are not present elsewhere.

Even though neglecting the added mass terms leads to large errors in the position of the flutter boundaries, sometimes with values of the relative error of 50% or above, the magnitude of these errors is not as large as that observed when comparing two different models. This seems to indicate that errors originated within a dynamic stall model due to the neglect of the added terms are often smaller than those associated with its modelling uncertainties.

This investigation has intentionally avoided the parameter settings which would result in a bifurcation close to the discontinuity. The value of the parameter α_1 is taken to be a constant so that the discontinuity can be explicitly defined, otherwise the discontinuity will be a function of the flow conditions. This makes the analysis of the dynamics very difficult, but also very interesting because the bifurcations which might occur in the neighbourhood of the discontinuity could be discontinuous.

Acknowledgements

The authors would like to thank Prof. Stefano Lenci of Università Politecnica delle Marche, Ancona, Italy, for useful discussions and our departmental colleague Dr Rafael Palacios Nieto for his insightful comments on an earlier version of the manuscript. We would also like to thank Prof. Stuart J. Price for providing us with a copy of some of his papers.

Appendix A. The system of ODEs describing the aeroelastic system

The purpose of this appendix is to present the governing equations of the aeroelastic model relevant to the calculation of flutter boundaries used here to assess the effect of the added mass terms. The system of ODEs that represents the full aeroelastic system corresponding to Eq. (15) is written here as

$$\mathbf{x}' = \mathbf{f}(\mathbf{x}, \mathbf{x}'),$$

where the subindex f has been dropped for notational convenience.

Recall that the first twelve components of \mathbf{x} represent the aerodynamic states in the LB model and the other four correspond to the pitch and plunge structural degrees of freedom and their derivatives, i.e. $[x_{13}, x_{14}, x_{15}, x_{16}] = [\theta, \theta', \xi, \xi']$. The right-hand side of the system of 16 ODEs at a fixed point is given by $\mathbf{f} = [f_1, f_2, \dots, f_{16}]^T$ and its various components are described in the following.

A full description of our interpretation of the LB model, as well as a physical or mathematical interpretation of the variables involved and their relationships in the state-space version of the LB model, is described by Chantharasanawong (2007) and Galvanetto et al. (2008). We refer the reader to these references for any queries about the model not covered by this article. Alternatively, the interested reader could also consult the original papers by Leishman and Beddoes, namely Beddoes (1976, 1983, 1984), Leishman and Beddoes (1986, 1989), Leishman and Nguyen (1988), Crouse and Leishman (1992), that we have used to construct our version of the LB model.

The first nine components of \mathbf{f} correspond to the linear aerodynamic terms and are written as

$$f_1 = \left(\frac{c}{2V}\right) \left(a_{11}x_1 + \alpha + \frac{1}{2}q\right), \quad f_2 = \left(\frac{c}{2V}\right) \left(a_{22}x_2 + \alpha + \frac{1}{2}q\right),$$

$$f_3 = \left(\frac{c}{2V}\right) (a_{33}x_3 + \alpha), \quad f_4 = \left(\frac{c}{2V}\right) (a_{44}x_4 + q),$$

$$f_5 = \left(\frac{c}{2V}\right) (a_{55}x_5 + \alpha), \quad f_6 = \left(\frac{c}{2V}\right) (a_{66}x_6 + \alpha),$$

$$f_7 = \left(\frac{c}{2V}\right)(a_{77}x_7 + q), \quad f_8 = \left(\frac{c}{2V}\right)(a_{88}x_8 + q),$$

$$f_9 = \frac{1}{T_P} \left[(c_{11}x_1 + c_{12}x_2 + c_{13}x_3 + c_{14}x_4) + \frac{4}{M}\alpha + \frac{1}{M}q - x_9 \right],$$

where the effective angle of attack α and nondimensional pitch rate of the full system q are given by

$$\alpha = \tan^{-1}\left(\frac{U}{L}\right) = \alpha(x_{13}, x_{14}, x_{16}), \quad q = 2\frac{LU' - UL'}{U^2 + L^2} = q(x_{13}, x_{14}, x_{16}, x'_{14}, x'_{16}),$$

with

$$U = \sin(x_{13}) + x_{16}\cos(x_{13}) + x_{14}r, \quad L = \cos(x_{13}) - x_{16}\sin(x_{13}),$$

$$U' = x_{14}\cos(x_{13}) - x_{14}x_{16}\sin(x_{13}) + x'_{16}\cos(x_{13}) + x'_{14}r, \quad L' = -x_{14}\sin(x_{13}) - x_{14}x_{16}\cos(x_{13}) - x'_{16}\sin(x_{13}).$$

The coefficients for the linear aerodynamic terms are

$$a_{11} = -\frac{2V}{c}b_1\beta^2, \quad a_{22} = -\frac{2V}{c}b_2\beta^2, \quad a_{33} = -\frac{1}{K_x T_I}, \quad a_{44} = -\frac{1}{K_q T_I},$$

$$a_{55} = -\frac{1}{b_3 K_{xM} T_I}, \quad a_{66} = -\frac{1}{b_4 K_{xM} T_I}, \quad a_{77} = -\frac{2V}{c}b_5\beta^2, \quad a_{88} = -\frac{1}{K_{qM} T_I}$$

and

$$c_{11} = C_{N\alpha}^S \frac{2V}{c} \beta^2 A_1 b_1, \quad c_{12} = C_{N\alpha}^S \frac{2V}{c} \beta^2 A_2 b_2, \quad c_{13} = \frac{4}{M} \left(\frac{-1}{K_x T_I} \right),$$

$$c_{14} = \frac{1}{M} \left(\frac{-1}{K_q T_I} \right), \quad c_{21} = c_{11}(0.25 - x_{ac}), \quad c_{22} = c_{12}(0.25 - x_{ac}),$$

$$c_{25} = \frac{-1}{M} \left(\frac{-A_3}{b_3 K_{xM} T_I} \right), \quad c_{26} = \frac{-1}{M} \left(\frac{-A_4}{b_4 K_{xM} T_I} \right), \quad c_{27} = -\frac{C_{N\alpha}^S}{16} b_5 \beta^2 \left(\frac{2V}{c} \right),$$

$$c_{28} = \frac{-7}{12M} \left(\frac{-1}{K_{qM} T_I} \right),$$

where x_{ac} is the nondimensional position of the aerofoil aerodynamic centre. The time constants used in the expressions above are given by

$$K_q = \frac{0.75}{(1-M) + 2\pi\beta^2 M^2 (A_1 b_1 + A_2 b_2)},$$

$$K_{xM} = \frac{A_3 b_4 + A_4 b_3}{b_3 b_4 (1-M)}, \quad K_{qM} = \frac{7}{15(1-M) + 3\pi\beta M^2 b_5},$$

where $\beta^2 = 1 - M^2$ and the values of the coefficients are taken to be

$$A_1 = 0.30, \quad b_1 = 0.14, \quad A_2 = 0.70 = 1 - A_1, \quad b_2 = 0.53,$$

$$A_3 = 1.5, \quad b_3 = 0.25, \quad A_4 = -0.5 = 1 - A_3, \quad b_4 = 0.1, \quad A_5 = 1.0, \quad b_5 = 0.5.$$

The next three components of \mathbf{f} represent the nonlinear aerodynamic terms and are expressed as

$$f_{10} = \begin{cases} \frac{1}{T_{f0}} \left(1 - 0.30 \exp \left(\frac{\left| \frac{x_9}{C_{Nz}} \right| - \alpha_1}{S_1} \right) - x_{10} \right) & \text{if } \left| \frac{x_9}{C_{Nz}} \right| \leq \alpha_1, \\ \frac{1}{T_{f0}} \left(0.04 + 0.66 \exp \left(\frac{\alpha_1 - \left| \frac{x_9}{C_{Nz}} \right|}{S_2} \right) - x_{10} \right) & \text{if } \left| \frac{x_9}{C_{Nz}} \right| > \alpha_1, \end{cases}$$

$$f_{11} = -\frac{x_{11}}{T_{v0}},$$

$$f_{12} = \begin{cases} \frac{1}{F_1 T_{f0}} \left(1 - 0.30 \exp \left(\frac{|x_{13}| - \alpha_1}{S_1} \right) - x_{12} \right) & \text{if } |x_{13}| \leq \alpha_1, \\ \frac{1}{F_1 T_{f0}} \left(0.04 + 0.66 \exp \left(\frac{\alpha_1 - |x_{13}|}{S_2} \right) - x_{12} \right) & \text{if } |x_{13}| > \alpha_1 \end{cases}$$

with $F_1 = 0.63$.

Finally, the structural terms are given by

$$f_{13} = x_{14},$$

$$f_{14} = \frac{1}{b_0} \left[\frac{1}{(U^*)^2} (x_{13} - \theta_0) + \frac{2\zeta_\theta}{U^*} x_{14} - \frac{x_\theta}{r_\theta^2} \left(\frac{\bar{\omega}}{U^*} \right)^2 x_{15} - 2\zeta_\xi \frac{x_\theta}{r_\theta^2} \left(\frac{\bar{\omega}}{U^*} \right) x_{16} - \frac{x_\theta}{\pi \mu r_\theta^2} C_L - \frac{0.5 + a_h}{\pi \mu r_\theta^2} C_N - \frac{2}{\pi \mu r_\theta^2} C_M \right],$$

$$f_{15} = x_{16},$$

$$f_{16} = \frac{1}{b_0} \left[-\frac{x_\theta}{(U^*)^2} x_{13} - \frac{2\zeta_\theta x_\theta}{U^*} x_{14} + \left(\frac{\bar{\omega}}{U^*} \right)^2 x_{15} + 2\zeta_\xi \left(\frac{\bar{\omega}}{U^*} \right) x_{16} + \frac{1}{\pi \mu} C_L + \frac{(0.5 + a_h)x_\theta}{\pi \mu r_\theta^2} C_N + \frac{2x_\theta}{\pi \mu r_\theta^2} C_M \right],$$

with $b_0 = (x_\theta/r_\theta)^2 - 1$. Notice that here the aerodynamic coefficients used are C_L and C_N instead of the more classical C_L and C_D used in Eqs. (1) and (2). Nevertheless, they are related through a simple change of variables, namely $C_N = C_L \cos \alpha + C_D \sin \alpha$.

The aerodynamic coefficients representing force and moment can be exclusively expressed in terms of the state variables and are given by

$$C_L = \left(C_{Nz} \left(\frac{2V}{c} \right) \beta^2 (A_1 b_1 x_1 + A_2 b_2 x_2) \left(\frac{1 + \sqrt{x_{10}}}{2} \right)^2 + \frac{4}{M} (\alpha + a_{33} x_3) + \frac{1}{M} (q + a_{44} x_4) + x_{11} \right) \cos(x_{13}) \\ - \left(\eta C_{Nz} \left(\frac{2V}{c} \right) \beta^2 (A_1 b_1 x_1 + A_2 b_2 x_2) \sqrt{x_{10}} \right) \sin(x_{13}),$$

$$C_N = C_{Nz} \left(\frac{2V}{c} \right) \beta^2 (A_1 b_1 x_1 + A_2 b_2 x_2) \left(\frac{1 + \sqrt{x_{10}}}{2} \right)^2 + \frac{4}{M} (\alpha + a_{33} x_3) + \frac{1}{M} (q + a_{44} x_4) + x_{11},$$

$$C_M = C_{Nz} \frac{2V}{c} \beta^2 (A_1 b_1 x_1 + A_2 b_2 x_2) \frac{(1 + \sqrt{\hat{x}})^2}{4} (K_0 + K_1(1 - \hat{x}) + K_2 \sin(\pi \hat{x}^2)) \\ - \frac{1}{M} (A_3 a_{55} x_5 + A_4 a_{66} x_6 + \alpha) - \frac{7}{12M} \left(-\frac{1}{K_{qM} T_I} x_8 + q \right) - 0.25 \left(1 - \cos \left(\frac{\pi \tau_v}{T_{vl}} \right) \right) x_{11},$$

where

$$\hat{x} = \begin{cases} x_{10} & \text{if } x_{10} > x_{12}, \\ x_{12} & \text{if } x_{10} \leq x_{12}. \end{cases}$$

Table 1

Parameters of the LB model for a NACA0012 aerofoil as functions of the free-stream Mach number.

Mach number	0.30	0.4	0.5	0.6	0.7	0.75	0.8
$C_{N\alpha}^S$	6.6211	7.0502	7.5100	8.2457	9.6864	10.9432	13.6407
α_{10}	0.2529	0.2073	0.1741	0.1409	0.0929	0.0580	0.0116
$\delta\alpha_1$	0.0367	0.0349	0.0253	0.0175	0.0140	0.0035	0.0017
S_1	0.0262	0.0284	0.0305	0.0349	0.0393	0.0305	0.0061
S_2	0.0201	0.0140	0.0105	0.0061	0.0044	0.0070	0.0016
K_0	0.0125	0.0300	0.1000	0.1900	0.1500	0.0050	−0.0500
K_1	−0.108	−0.108	−0.100	−0.096	−0.072	−0.104	0.016
K_2	0.04	0.05	0.04	0.04	0.15	−0.02	−0.01
D_f	8.0	7.75	6.2	6.0	5.9	5.5	4.0
T_{f0}	3.0	2.5	2.2	2.0	2.0	2.0	2.0
T_P	1.7	1.8	2.0	2.5	3.0	3.3	4.3
T_{v0}	6.0	6.0	6.0	6.0	6.0	6.0	4.0
T_{vt}	5.25	6.75	6.75	6.75	6.75	6.75	6.75

The other parameters of the LB model for the NACA0012 aerofoil are functions of the Mach number M and are given in Table 1.

The entries of the 16×16 Jacobian matrix $\partial f/\partial x$ required for the flutter calculations presented here can be easily obtained from the above equations or consulted in Chantharasenawong (2007).

References

- Beddoes, T., 1976. A synthesis of unsteady aerodynamic effects including stall hysteresis. *Vertica* 1, 113–123.
- Beddoes, T., 1983. Representation of airfoil behaviour. *Vertica* 7 (2), 183–197.
- Beddoes, T., 1984. Practical computation of unsteady lift. *Vertica* 8 (1), 55–71.
- Beedy, J., Barakos, G., Badcock, K., Richards, B., 2003. Non-linear analysis of stall flutter based on the ONERA aerodynamic model. *Aeronautical Journal*, 495–509.
- Blevins, R.D., 2001. *Flow-induced Vibration*, second ed. Krieger Pub. Co., Malabar, Florida.
- Chantharasenawong, C., 2007. Nonlinear aeroelastic behaviour of aerofoils under dynamic stall. Ph.D. Thesis, Department of Aeronautics, Imperial College London.
- Crouse, G.J., Leishman, J., 1992. Transonic aeroelasticity analysis using state-space unsteady aerodynamic modeling. *Journal of Aircraft* 29 (1), 153–160.
- Dat, R., Tran, C., 1983. Investigation of the stall flutter of an airfoil with a semi-empirical model of 2-D flow. *Vertica* 7 (2), 73–86.
- Fung, Y.C., 1993. *An Introduction to the Theory of Aeroelasticity*. Dover, New York.
- Galvanetto, U., Peiró, J., Chantharasenawong, C., 2007. Remarks on the nonlinear dynamics of a typical aerofoil section in dynamic stall. *Aeronautical Journal* 111 (1125), 731–739.
- Galvanetto, U., Peiró, J., Chantharasenawong, C., 2008. An assessment of the effect of non-smoothness of the Leishman–Beddoes dynamic stall model on the nonlinear dynamics of a typical aerofoil section. *Journal of Fluids and Structures* 24, 151–163.
- Guckenheimer, J., Holmes, P., 2002. *Nonlinear oscillations, dynamical systems, and bifurcations of vector fields*. Applied Mathematical Sciences, vol. 42. Springer, New York.
- Hansen, M.H., Gaunaa, M., Madsen, H.A., June 2004. A Beddoes–Leishman type dynamic stall model in state-space and indicial formulation. Technical Report RISO-R-1354, Risø National Laboratory, Roskilde, Denmark.
- Lee, B., Price, S., Wong, Y., 1999. Nonlinear aeroelastic analysis of airfoils: bifurcation and chaos. *Progress in Aerospace Sciences* 35, 205–334.
- Leishman, J., 2006. *Principles of Helicopter Aerodynamics*, second ed. Cambridge.
- Leishman, J., Beddoes, T., 1986. A generalised model for airfoil unsteady aerodynamic behaviour and dynamic stall using the indicial method. In: *Proceedings of the 42nd Annual Forum of the American Helicopter Society*, Washington, DC.
- Leishman, J., Beddoes, T., 1989. A semi-empirical model for dynamic stall. *Journal of the American Helicopter Society* 34, 3–17.
- Leishman, J., Nguyen, K., 1988. State-space representation of unsteady airfoil behaviour. *AIAA Journal* 28 (5), 836–844.
- Li, X., Fleeter, S., 2003. Dynamic stall generated airfoil oscillations. *International Journal of Turbo and Jet Engines* 20, 217–233.
- Mahajan, A., Kaza, K., Dowell, E., 1993. Semi-empirical model for prediction of unsteady forces on an airfoil with application to flutter. *Journal of Fluids and Structures* 7, 87–103.
- McAlister, K., Pucci, W., McCroskey, W., Carr, L., September 1983. An experimental study of dynamic stall on advanced airfoil sections; volume 2 pressure and force data. NASA Technical Memorandum TM-84245.

- McCroskey, W., Carr, L., McAlister, K., 1976. Dynamic stall experiments on oscillating airfoils. *AIAA Journal* 14 (1), 57–63.
- Price, S., Fragiskatos, G., 19–22 June 2000. Nonlinear aeroelastic response of a two-degree-of-freedom airfoil oscillating in dynamic stall. In: Ziada, S., Staubli, T. (Eds.), 7th International Conference on Flow Induced Vibration, Lucerne, Switzerland. A.A. Balkema, Rotterdam, pp. 437–444.
- Price, S., Keleris, J., 1996. Non-linear dynamics of an airfoil forced to oscillate in dynamic stall. *Journal of Sound and Vibration* 194 (2), 265–283.
- Sarkar, S., Bijl, H., 2008. Nonlinear aeroelastic behaviour of an oscillating airfoil during stall-induced vibration. *Journal of Fluids and Structures* 24, 757–777.
- Tang, D., Dowell, E., 1996. Comments on the ONERA stall aerodynamic model and its impact on aeroelastic stability. *Journal of Fluids and Structures* 10 (4), 353–366.
- Tran, C., Petot, D., 1981. Semi-empirical model for the dynamic stall of airfoils in view to the application to the calculation of responses of a helicopter blade in forward flight. *Vertica* 5, 35–53.